# THE ARCTIC CLOUD PUZZLE

## Using ACLOUD/PASCAL Multiplatform Observations to Unravel the Role of Clouds and Aerosol Particles in Arctic Amplification

Manfred Wendisch, Andreas Macke, André Ehrlich, Christof Lüpkes, Mario Mech, Dmitry Chechin, Klaus Dethloff, Carola Barrientos Velasco, Heiko Bozem, Marlen Brückner, Hans-Christian Clemen, Susanne Crewell, Tobias Donth, Regis Dupuy, Kerstin Ebell, Ulrike Egerer, Ronny Engelmann, Christa Engler, Oliver Eppers, Martin Gehrmann, Xianda Gong, Matthias Gottschalk, Christophe Gourbeyre, Hannes Griesche, Jörg Hartmann, Markus Hartmann, Bernd Heinold, Andreas Herber, Hartmut Herrmann, Georg Heygster, Peter Hoor, Soheila Jafariserajehlou, Evelyn Jäkel, Emma Järvinen, Olivier Jourdan, Udo Kästner, Simonas Kecorius, Erlend M. Knudsen, Franziska Köllner, Jan Kretzschmar, Luca Lelli, Delphine Leroy, Marion Maturilli, Linlu Mei, Stephan Mertes, Guillaume Mioche, Roland Neuber, Marcel Nicolaus, Tatiana Nomokonova, Justus Notholt, Mathias Palm, Manuela van Pinxteren, Johannes Quaas, Philipp Richter, Elena Ruiz-Donoso, Michael Schäfer, Katja Schmieder, Martin Schnaiter, Johannes Schneider, Alfons Schwarzenböck, Patric Seifert, Matthew D. Shupe, Holger Siebert, Gunnar Spreen, Johannes Stapf, Frank Stratmann, Teresa Vogl, André Welti, Heike Wex, Alfred Wiedensohler, Marco Zanatta, and Sebastian Zeppenfeld

**Employing two research aircraft, one icebreaking research vessel, an ice floe camp including an instrumented tethered balloon, and a permanent ground-based measurement station at Spitsbergen, a consortium of polar scientists combined observational forces in a field campaign of unprecedented complexity to uncover the secrets of clouds and their role in Arctic amplification.**

Currently, we are witnessing drastic climate changes in the Arctic that are unprecedented in the history of mankind (Jeffries et al. 2013). Within about the last 40 years, the Arctic sea ice extent has decreased dramatically (Stroeve et al. 2012); in particular, the September minimum of sea ice extent dropped by almost two-thirds. The maximum extent of winter sea ce has shrunk significantly as well (Onarheim et al. 2018). In March 2017 the Arctic maximum sea ice extent decreased to its smallest value ever recorded (Richter-Menge et al. 2017). Also, the thickness of the sea ice has declined. Multiyear thick sea ice made up only 21% of the sea ice cover in 2017; in 1985 this value was about 45% (Richter-Menge et al. 2017). Because thin ice melts faster than thick ice, the thin ice gets thinner and a positive feedback occurs.

Concurrently, the Arctic near-surface temperature considerably increased within the last three to four decades, and it continues to rise at double the rate of global average values—a phenomenon commonly called Arctic amplification (Serreze and Barry 2011). In 2017 the mean Arctic near-surface air temperature over land exceeded the 1981–2010 average by 1.6°C, which is (after 2016) the second-highest average ever ▶

Overflight over the R/V *Polarstern* with the research aircraft Polar 5 over the Marginal Ice Zone (MIZ) north of Svalbard during the combined ACLOUD/PASCAL campaign.

recorded (Richter-Menge et al. 2017). As a result the melting season starts earlier and the freeze-up begins later. For example, the freeze-up in 2016 in the Barents and Kara Seas was among the latest ever reported. It is evident that the winter season is becoming particularly impacted by Arctic warming.

Unfortunately, we neither fully comprehend these striking climate changes in the Arctic nor understand why they happen so fast. As a result we are unable to reliably predict how the Arctic climate will evolve in the future (Screen et al. 2018). Even worse, we cannot evaluate the substantial consequences a warming and thawing Arctic might have for midlatitude weather (Cohen et al. 2014; Walsh 2014; Cohen et al. 2018). Therefore, several international efforts are underway to improve model projections of the Arctic climate, such as the Polar Prediction Project and the Year of Polar Prediction (Jung et al. 2016). However, models alone will not resolve the Arctic climate issue. They often use simple parameterizations, which need to be verified, tested, and improved by measurements. The required observations are still sparsely distributed across the Arctic. As a consequence further data should be collected in well-planned and dedicated campaigns to document and understand the Arctic climate changes. Such observations are costly and require tremendous organizational efforts, including the logistics (aircraft, icebreaker, etc.), which are challenging in the harsh environmental conditions in the Arctic.

Advances in land-based observations [e.g., obtained by the work of the International Arctic Systems for Observing the Atmosphere (IASOA)] help to provide important insights into the changing Arctic climate system (Uttal et al. 2016). However, targeted observations that focus on special Arctic phenomena [such as mixed-phase clouds, stable atmospheric boundary layer (ABL), polar day and night, high surface reflectivity] are needed to clarify key elements that are thought to contribute to the Arctic amplification phenomenon (Wendisch et al. 2017). This should also include relevant processes such as airmass transformations during meridional transport (Pithan et al. 2018). For this purpose it is essential to organize concerted observational campaigns looking at certain aspects of the changing Arctic system, such as the Multidisciplinary Drifting Observatory for the Study of Arctic Climate (MOSAiC) campaign, which is planned for 2019/20 (www.mosaic-expedition.org). Furthermore, it is crucial to implement sustained research programs, such as the German Arctic Amplification: Climate Relevant Atmospheric and Surface Processes, and Feedback Mechanisms [$(AC)^3$; www.ac3-tr.de/] project, that orchestrate observations and modeling efforts (Wendisch et al. 2017).

Because the current changes of the Arctic climate system happen so fast, it is likely that atmospheric processes play a major role. Therefore, a large number of previous airborne and ship-based campaigns were particularly focused on atmospheric and surface

**AFFILIATIONS:** Wendisch, Ehrlich, Brückner, Donth, Engler, Gottschalk, Jäkel, Kretzschmar, Quaas, Ruiz-Donoso, Schäfer, and Stapf—Leipziger Institut für Meteorologie, Universität Leipzig, Leipzig, Germany; Macke, Barrientos Velasco, Egerer, Engelmann, Gong, Griesche, M. Hartmann, Heinold, Herrmann, Kästner, Kecorius, Mertes, van Pinxteren, Schmieder, Seifert, Siebert, Stratmann, Vogl, Welti, Wex, Wiedensohler, and Zeppenfeld—Leibniz-Institut für Troposphärenforschung, Leipzig, Germany; Lüpkes, Chechin, Dethloff, Gehrmann, J. Hartmann, Herber, Maturilli, Neuber, Nicolaus, and Zanatta—Alfred-Wegener-Institut, Helmholtz-Zentrum für Polar- und Meeresforschung (AWI), Bremerhaven, Germany; Mech, Crewell, Ebell, Knudsen, and Nomokonova—Institut für Geophysik und Meteorologie, Universität zu Köln, Cologne, Germany; Bozem and Hoor—Institut für Physik der Atmosphäre, Johannes Gutenberg-Universität, Mainz, Germany; Eppers—Institut für Physik der Atmosphäre, Johannes Gutenberg-Universität, and Particle Chemistry Department, Max Planck Institute for Chemistry, Mainz, Germany; Clemen, Köllner, and Schneider—Particle Chemistry Department, Max Planck Institute for Chemistry, Mainz, Germany; Heygster, Jafariserajehlou, Lelli, Mei, Notholt, Palm, Richter, and Spreen—Institut für Umweltphysik, Universität Bremen, Bremen, Germany; Järvinen and Schnaiter— Institut für Meteorologie und Klimaforschung, Karlsruher Institut für Technologie, Karlsruhe, Germany; Dupuy, Gourbeyre, Jourdan, Leroy, Mioche, and Schwarzenböck—Laboratoire de Météorologie Physique, Université Clermont Auvergne/OPGC/CNRS, UMR 6016, Clermont-Ferrand, France; Shupe—Earth System Research Laboratory, National Oceanic and Atmospheric Administration, and Cooperative Institute for Research in the Environmental Sciences, University of Colorado Boulder, Boulder, Colorado

**CORRESPONDING AUTHOR:** Manfred Wendisch, m.wendisch@uni-leipzig.de

*The abstract for this article can be found in this issue, following the table of contents.*

DOI:10.1175/BAMS-D-18-0072.1

A supplement to this article is available online (10.1175/BAMS-D-18-0072.

In final form 30 October 2018

processes, partly neglecting the long-term effects of the slowly changing ocean. Several examples of these previous efforts are discussed in the sidebar "Previous airborne and ship-based campaigns in the Arctic," which is summarized in Table 1 (including respective references), to provide context for new observations.

These past campaigns generally highlighted the important role that clouds can—and do— play in that changing system and in the manifestation of Arctic amplification. However, there is still a basic lack of understanding of the interplay between aerosol particles, clouds, and surface properties, as well as turbulent and radiative fluxes with dynamical processes, that currently prevents accurately simulating clouds in the Arctic climate system. The sidebar "The Arctic Cloud Puzzle" introduces the puzzling problems related to Arctic clouds in more detail.

To enhance the existing knowledge on the role of Arctic clouds and aerosol particles in the Arctic climate system, and thereby to help to further solve this Arctic cloud puzzle, two concerted field studies have been performed: Arctic Cloud Observations Using Airborne Measurements during Polar Day (ACLOUD) and Physical Feedbacks of Arctic Boundary Layer, Sea Ice, Cloud and Aerosol (PASCAL). The jointly planned and organized observations took place around Svalbard, Norway, in May and June 2017. ACLOUD consisted of airborne observations by two research aircraft, Polar 5 and Polar 6 (Wesche et al. 2016). PASCAL involved measurements from the Research Vessel (R/V) *Polarstern* (Knust 2017) and an ice floe camp [including the Balloon-bornE moduLar Utility for profilinG the lower Atmosphere (BELUGA) tethered balloon]. A detailed summary of the measurements performed during PASCAL can be found in Macke and Flores (2018). Additionally, measurements from the permanent joint research base operated by Alfred Wegener Institute (AWI) and the French Polar Institute Paul-Émile Victor (IPEV; AWIPEV) at Ny-Ålesund (Svalbard) were involved (Neuber 2006). The ACLOUD and PASCAL campaigns are unique in that both were tightly coordinated under the collaborative $(AC)^3$ program (Wendisch et al. 2017), funded by the German

## PREVIOUS AIRBORNE AND SHIP-BASED CAMPAIGNS IN THE ARCTIC

MIZEX West (1983) and MIZEX East (1984) were aimed at understanding the effects of the marginal ice zone (MIZ) with a focus on air–ice–sea exchange processes. Both projects were large international campaigns that were conducted with several ships and aircraft. REFLEX I, II, and III focused on i) the influence of the MIZ on transfer coefficients, ii) the cloud impact on radiation flux densities as well as the parameterizations of the surface albedo as a function of sea ice fraction and solar zenith angle, and iii) the investigation of cold-air outbreaks. IAOE focused on the potential climatic control of dimethyl sulfide (DMS). The main goal of the comprehensive SHEBA campaign was to study the surface heat and energy budget of the sea ice–covered ocean, based on continuous and mostly shipborne measurements over one year at a station drifting in the Beaufort Gyre. ARTIST pursued goals similar to REFLEX but with a dedicated focus on airborne turbulence measurements in cold-air outbreaks. The ASTAR I, II, and III series of airborne campaigns investigated aerosol–cloud interactions and the resulting modifications of radiative properties of clouds. Fram Strait cyclones and their impact on sea ice development were studied during the FRAMZY series of observations carried out with buoys and aircraft. The AOE campaign investigated summer meteorological conditions and clouds. M-PACE merged the observations of two stationary ground-based sites and two aircraft to study physical processes in Arctic mixed-phase clouds. ISDAC investigated aerosol–cloud interactions in the ABL. Two POLARCAT campaigns operated from northern Sweden and Kangerlussuaq (Greenland) during the International Polar Year (2008). ARCPAC was an airborne campaign coordinated with POLARCAT; it was closely collocated with remote sensing and in situ observations from the ground site of Barrow, Alaska (now known as Utqiaġvik). ASCOS also focused on late summer cloud–aerosol interactions in the central Arctic. MELTEX concentrated on the importance of melt ponds on surface albedo during the initial stage of sea ice melt. IceBridge uses airborne instruments to obtain maps of ice sheets, ice shelves, and sea ice of Arctic and Antarctic areas once a year. ARCTAS studied the influx of midlatitude pollution, boreal forest fires, aerosol radiative forcing, and chemical processes. A series of airborne research campaigns using the Polar 5 and Polar 6 research aircraft was conducted out of Svalbard and Inuvik (northern Canada) during SORPIC, VERDI, and RACEPAC. These measurements investigated aerosol–cloud–radiation interactions. ACCACIA was conducted to measure aerosol and cloud effects on the Arctic surface energy balance and climate. STABLE mainly investigated the impact of leads on the ABL and cold-air outbreaks with a focus on the flow between the inner Arctic and the marginal sea ice zone. NETCARE focused on carbonaceous aerosol, ice cloud formation and impact, and ocean–atmosphere interactions. ARISE collected airborne data on clouds, atmospheric radiation, and sea ice properties between the sea ice minimum in September and the beginning of refreezing in late autumn. ACSE looked at Arctic clouds in summer. N-ICE studied how the rapid shift to a younger and thinner sea ice regime in the Arctic affects energy fluxes and sea ice dynamics.

**Table 1. Examples of major campaigns focused on atmospheric and surface processes performed in the Arctic; the list is not complete.**

| Full name | Acronym | Year | Area | Airborne | Ship based | Selected references |
|---|---|---|---|---|---|---|
| Marginal Ice Zone Experiment West | MIZEX West | 1983 | Bering Sea | ✓ | ✓ | Cavalieri et al. (1983) |
| Marginal Ice Zone Experiment East | MIZEX East | 1984 | Greenland Sea | ✓ | ✓ | MIZEX Group (1986) |
| Radiation and Energy Flux Experiments I, II, III | REFLEX I, II, III | 1991, 1993, 1995 | Fram Strait | ✓ | ✓ | Hartmann et al. (1992, 1994)<br>Kottmeier et al. (1994)<br>Freese and Kottmeier (1998) |
| International Arctic Ocean Expedition | IAOE | 1991 | Central Arctic | | ✓ | Leck et al. (1996) |
| Surface Heat Budget of the Arctic Ocean | SHEBA | 1997/98 | Beaufort Sea | ✓ | ✓ | Curry et al. (2000)<br>Uttal et al. (2002)<br>Perovich et al. (2003)<br>Shupe et al. (2006)<br>Verlinde et al. (2007) |
| Arctic Radiation and Turbulence Interaction Study | ARTIST | 1998 | Fram Strait | ✓ | | Hartmann et al. (1999)<br>Gryanik and Hartmann (2002)<br>Gryanik et al. (2005) |
| Arctic Study of Aerosol, Clouds and Radiation I, II, III | ASTAR I, II, III | 2000, 2004, 2007 | Svalbard | ✓ | | Special issue of *Atmos. Chem. Phys.*[a] |
| Fram Strait Cyclones and Their Impact on Sea Ice | FRAMZY | 1999, 2002, 2007, 2008, 2009 | Fram Strait | ✓ | | Brümmer et al. (2008)<br>Collection of papers[b] |
| Arctic Ocean Experiment | AOE | 1996, 2001 | Central Arctic Ocean | | ✓ | Tjernström et al. (2004) |
| Mixed-Phase Arctic Cloud Experiment | M-PACE | 2004 | Alaska | ✓ | | Verlinde et al. (2007) |
| Indirect and Semidirect Aerosol Campaign | ISDAC | 2008 | Alaska | ✓ | | McFarquhar et al. 2011) |
| Polar Study Using Aircraft, Remote Sensing, Surface Measurements and Models of Climate, Chemistry, Aerosols, and Transport | POLARCAT | 2008 | Sweden, Greenland | ✓ | ✓ | Delanoe et al. (2013)<br>Law et al. (2014) |
| Aerosol, Radiation, and Cloud Processes Affecting Arctic Climate | ARCPAC | 2008 | Barrow, Alaskan Arctic | ✓ | | Brock et al. (2011) |
| Arctic Summer Cloud Ocean Study | ASCOS | 2008 | Central Arctic | | ✓ | Tjernström et al. (2014)<br>Shupe et al. (2013)<br>Sedlar and Shupe 2014) |
| Melt Ponds on Energy and Momentum Fluxes between Atmosphere and Ocean | MELTEX | 2008 | Beaufort Sea | ✓ | | Rösel and Kaleschke (2012) |
| Arctic Research of the Composition of the Troposphere from Aircraft and Satellites | ARCTAS<br>IceBridge | 2008<br>2009–16 | Alaska<br>Western Arctic Ocean | ✓<br>✓ | | Jacob et al. (2010)<br>Kurtz et al. (2013) |
| Solar Radiation and Phase Discrimination of Arctic Clouds | SORPIC | 2010 | Svalbard | ✓ | | Bierwirth et al. (2013) |

Continued on next page

**Table 1. Continued.**

| Full name | Acronym | Year | Area | Airborne | Ship based | Selected references |
|---|---|---|---|---|---|---|
| Vertical Distribution of Ice in Arctic Clouds | VERDI | 2012 | Inuvik | ✓ | | Joint special issue: *Atmos. Meas. Tech.* *Atmos. Chem. Phys.*[c] |
| Aerosol–Cloud Coupling and Climate Interactions in the Arctic | ACCACIA | 2013 | Svalbard | ✓ | | Lloyd et al. (2015); Jones et al. (2018) |
| Spring Time Atmospheric Boundary Layer Experiment | STABLE | 2013 | Fram Strait | ✓ | | Tetzlaff et al. (2014, 2015) |
| Network on Climate and Aerosols: Addressing Key Uncertainties in Remote Canadian Environments | NETCARE | 2013, 2014, 2015 | Central Arctic | ✓ | | Collection of papers[d] |
| Radiation–Aerosol–Cloud Experiment in the Arctic Circle | RACEPAC | 2014 | Inuvik | ✓ | | Costa et al. (2017) |
| Arctic Radiation IceBridge Sea and Ice Experiment | ARISE | 2014 | Alaska | ✓ | | Smith et al. (2017) |
| Arctic Clouds in Summer Experiment | ACSE | 2014 | Eastern Arctic Ocean | | ✓ | Sotiropoulou et al. (2016) |
| | | | Along Russian Coast | | ✓ | Tjernström et al. (2015) |
| Norwegian Young Sea Ice Cruise | N-ICE | 2015 | North of Svalbard | | ✓ | Special section in *J. Geophys. Res. Oceans*[e] |
| Aerosol–Arctic Cloud Observations Using Airborne Measurements during Polar Day and Physical Feedbacks of Arctic Boundary Layer, Sea Ice, Cloud | ACLOUD/ PASCAL | 2017 | Svalbard | ✓ | ✓ | This paper |

[a] Please see www.atmos-chem-phys.net/special_issue151.html.

[b] Please see https://cera-www.dkrz.de/WDCC/ui/cerasearch/q?query=FRAMZY&page=0&rows=15.

[c] Please see www.atmos-meas-tech.net/special_issue10_362.html.

[d] Please see www.atmos-chem-phys.net/special_issue835.html.

[e] Please see http://agupubs.onlinelibrary.wiley.com/hub/issue/10.1002/(ISSN)2169-9291.NICE1/.

Research Foundation [Deutsche Forschungsgemeinschaft (DFG)]. From the beginning, modeling needs and perspectives guided the design and planned analyses from a unique set of closely collocated airborne (aircraft, tethered balloon), ground-based (ship, ground station), and satellite observations.

The general strategy of the measurements as well as the meteorological, sea ice, and cloud conditions during ACLOUD/PASCAL are introduced in the following section. The measured and retrieved quantities collected during the campaigns are briefly explained in the "Measured quantities and major instrumentation" section, while most of the details, in particular with respect to the instruments, are given in a separate online supplement (https://doi.org/10.1175/BAMS-D-18-0072.2). Then two illustrative examples of collocated measurements are presented to demonstrate the potential of the combined datasets. The major part of the paper ("Four pieces of the Arctic cloud puzzle") discusses selected measurement cases to investigate four pieces of the Arctic cloud puzzle. Finally, in the "Summary and open questions" section, a summary of the paper is given, including questions to be answered in the forthcoming data analyses of the ACLOUD and PASCAL campaigns and future research activities.

## INTRODUCTION OF ACLOUD AND PASCAL CAMPAIGNS.

*Complementary cloud observations.* The general measurement approach of ACLOUD and PASCAL is depicted in Fig. 1. One aircraft (Polar 5) was used as a remote sensing platform observing the clouds from above, while the other aircraft (Polar 6) went into and below the

clouds. Ground-based observations of the whole vertical column of cloud and aerosol particles were performed at the R/V *Polarstern* (ship and ice floe camp) and at Ny-Ålesund, mainly using remote sensing techniques. This was complemented by ABL (in situ) measurements at both sites. For example, the BELUGA tethered balloon was operated from the ice floe camp; it served as a linkage between the aircraft and the ground-based observations. In addition, aircraft underflights of the A-Train satellites (Stephens et al. 2018) provided context for the two campaigns. These satellite data are not discussed in this paper; they will be analyzed in forthcoming publications on ACLOUD/PASCAL. The time period of the ACLOUD and PASCAL campaigns extended from 23 May to 26 June 2017, defined by the full length of aircraft activities. The ice floe camp was set up between 5 and 14 June 2017.

Each aircraft completed 19 measurement flights (165 flight hours in total), of which 16 were coordinated flights between the two aircraft. The horizontal flight paths of the aircraft and the track of the R/V *Polarstern* are shown in Fig. 2. Table 2 summarizes all aircraft and tethered balloon flights. Ten coordinated aircraft flights were performed above the R/V *Polarstern*, while 13 occurred over the Ny-Ålesund site, and 6 were carried out underneath the *CloudSat/Cloud–Aerosol Lidar and Infrared Pathfinder Satellite Observations* (*CALIPSO*) satellite tracks (Stephens et al. 2018). The tethered balloon operation was coordinated with the aircraft and ship sampling during the ice floe camp. A total of 16 balloon flights were conducted.

*Synoptic, cloud, and sea ice conditions.* SYNOPTIC SITUATION. The synoptic conditions encountered

## THE ARCTIC CLOUD PUZZLE

Arctic clouds are a challenging puzzle, both within the Arctic climate system and through their role in Arctic amplification. First and foremost, clouds are a major modulator of the Arctic energy flow and surface energy budget. Because of low (or absent) sun in the Arctic, a highly reflective surface, the widespread existence of mixed-phase clouds, and frequent temperature inversions, the net radiative effect of Arctic low-level clouds warms the surface, except for during a short period in midsummer, when the sun is at its highest over regions with low surface albedo (Intrieri et al. 2002; Wendisch et al. 2013). The cloud warming effect is a peculiarity of Arctic low-level clouds: globally, this type of cloud has on average a cooling effect on the surface (Raschke et al. 2016). The net cloud impact on the surface and atmosphere is ultimately determined by cloud longevity and phase partitioning, which are controlled by a complex web of coupled microphysical, radiative, and dynamical processes (Morrison et al. 2012).

Radiatively opaque clouds, often containing liquid water and ice at temperatures below the freezing point, have been shown to impart the strongest radiative impact on the Arctic system (Shupe and Intrieri 2004; Stramler et al. 2011; Miller et al. 2015). However, these so-called mixed-phase clouds are not expected to persist for long periods as a result of the inherent instability of liquid water in close proximity to ice, which would typically lead to a total glaciation of the cloud (Wegener–Bergeron–Findeisen process) and a decrease in cloud radiative effects. Nevertheless, observations and modeling studies demonstrate how a multitude of feedback mechanisms between local and larger-scale processes can allow Arctic mixed-phase clouds to persist for periods of 3–5 days or longer (Shupe et al. 2006; Morrison et al. 2012). While many of the fundamental processes for forming and sustaining these important clouds are known, the manner in which they interact, feedback, and balance each other in such a delicate way is not clear nor well represented by numerical models.

Certain related processes are in need of further study. For example, the spatial distribution of cloud phase, both vertically and horizontally, is suspected to play a key role in sustaining clouds and in determining their impact on atmospheric radiation (Ehrlich et al. 2009). Additionally, the interaction between cloud radiation and atmospheric advection of moisture and temperature is not well understood (Pithan et al. 2018). The resulting atmospheric turbulence and cloud-scale dynamics can be important for determining the vertical structure and mixing of the atmospheric boundary layer, which feeds back on moisture sources and sinks for cloud maintenance. Finally, the role of aerosols and their effect on cloud composition is a particularly uncertain aspect of the puzzle. Arctic aerosol in situ data are sparse and originate mainly from permanent ground-based measurement stations, which are often influenced by free-tropospheric or large-scale advection (Freud et al. 2017). Observation-based understanding is also needed of aerosol properties over the open Arctic Ocean, marginal ice zone, and consolidated pack ice.

Jointly these processes comprise the broader Arctic cloud puzzle and have guided the research of ACLOUD/PASCAL, as the puzzle focuses on high-priority areas. The section on "Four pieces of the Arctic cloud puzzle" discusses cloud properties, the aerosol impact on clouds, atmospheric radiation, and turbulent dynamical processes. Importantly, research on these themes must address their interactions, how they collectively participate in Arctic amplification, and how Arctic cloud processes may further respond to a changing Arctic system.

during the combined ACLOUD/PASCAL campaigns are described in detail by Knudsen et al. (2018). Three key periods were distinguished: a cold period (CP; 23–29 May 2017), followed by a warm period (WP; 30 May–12 June 2017), and a normal period (NP; 13–26 June 2017). During the CP, cold and dry air from the north dominated the measurement area (Knudsen et al. 2018). This cold-air outbreak is considered unusual for this late period in spring and, at large scale, was associated with a relatively strongly positive phase of the Arctic dipole circulation pattern and a neutral Arctic Oscillation. Afterward, two weeks of moist air intrusions from the south and east determined the synoptic patterns around Svalbard (WP). During the final two weeks of the campaign, a mixture of airmass types prevailed (NP).

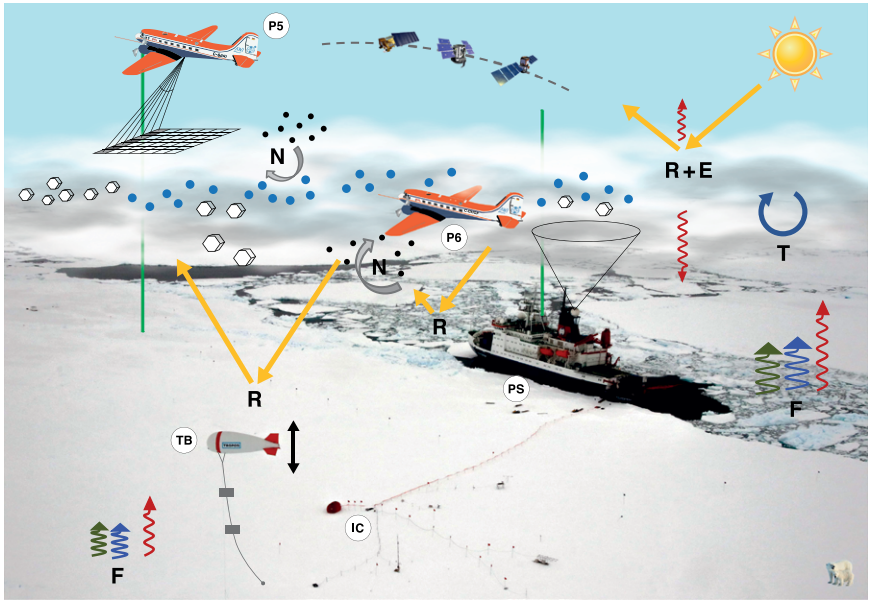


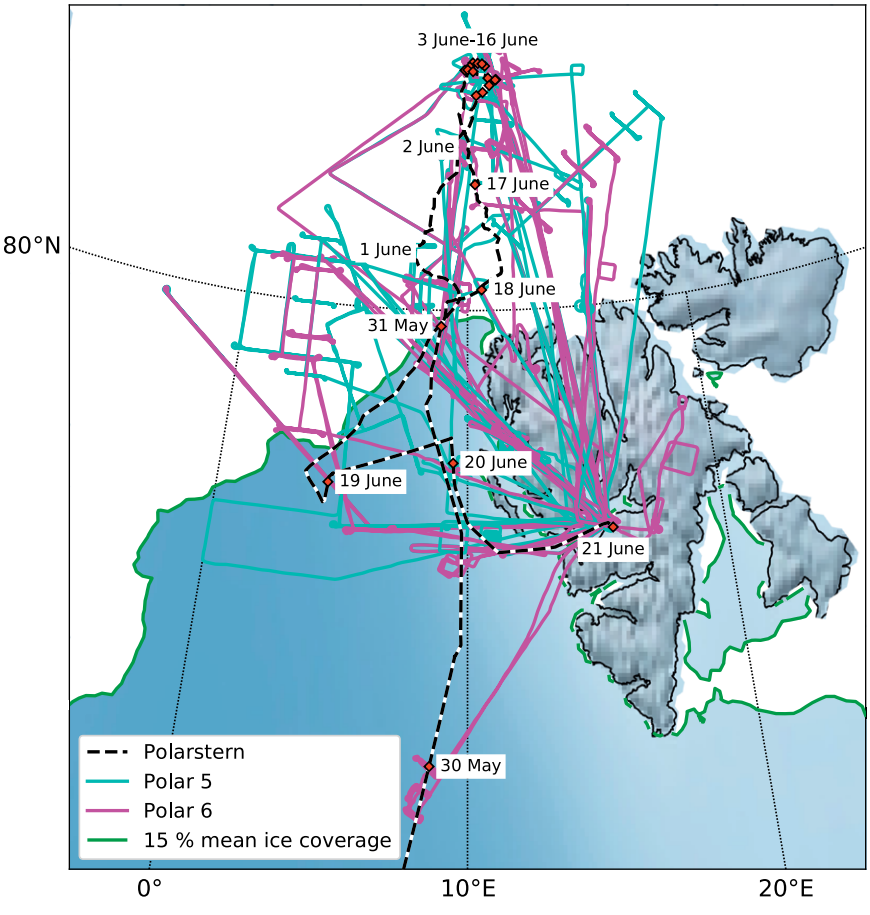


**Fig. 1 (top). Multiplatform measurement setup during the ACLOUD/PASCAL campaigns. Observations were performed from the ground using R/V *Polarstern* (PS) and an ice floe camp (IC) close to R/V *Polarstern*, including a tethered balloon (TB). Two aircraft were used: Polar 5 (P5) and Polar 6 (P6). Collocated underflights of satellites were carried out. The two green vertical lines indicate the lidar, the pixel field below P5 the imaging spectrometers, and the vertical cone from PS the radar. The A-train satellite constellation is indicated by the dashed line with the three schematics of *Aqua*, *CloudSat*, and *CALIPSO* at the top of the figure. Other abbreviations include R: reflection, E: emission, T: turbulence, F: energy fluxes (radiation, momentum, heat), N: entrainment.**

**Fig. 2 (bottom). Flight paths (light blue for Polar 5 aircraft, pink for Polar 6 aircraft) and R/V *Polarstern* ship track (black and white line) during the ACLOUD/PASCAL campaigns. The green line indicates the 15% ice cover averaged throughout the campaigns from 23 May to 26 Jun 2017. The dates in the white boxes mark the time of the position of R/V *Polarstern*.**

Cloud occurrence during the campaigns. To generally characterize the cloud conditions during ACLOUD/PASCAL, Fig. 3 shows time series of daily mean values of cloud-top height and cloud fraction as derived from different sources (satellite and aircraft data). Figure 3a shows the cloud-top height of the observed clouds with a top altitude below 3 km. In the following we call these clouds low-level clouds. The three synoptic periods (CP, WP, and NP) can clearly be distinguished. During the first two periods (CP, WP) of the ACLOUD and PASCAL campaigns (until 12 June 2017), the cloud-top height slightly decreased, which was caused by the shift from northerly cold air to southerly warm and moist air advection. The third period (NP) was dominated by mostly higher and more variable low-level cloud fields. Figure 3a allows a comparison of the mean cloud-top height, measured along the flight track by lidar on the Polar 5 aircraft (diamonds), and corresponding Moderate Resolution Imaging Spectroradiometer (MODIS) data (boxes with whiskers), processed for the entire area of operation during ACLOUD/PASCAL. Although such a comparison is partly selective as a result of different sampling strategies (measurements collected along a flight path of an aircraft are compared

**Table 2. Summary of flights with the Polar 5 and Polar 6 aircraft and the BELUGA tethered balloon performed during the ACLOUD/PASCAL campaigns. Takeoff and landing times are in UTC. PS: R/V *Polarstern*; P5: Polar 5 aircraft; P6: Polar 6 aircraft. Instrument settings on tethered balloon: So: ultrasonic anemometer, Hw: hot wire anemometer, B1/B2: broadband sensors, Sp: spectrometer, Ae: aerosol sampler. TKE: turbulent kinetic energy. Times are in UTC.**

| Date in 2017 | AIRCRAFT | | | TETHERED BALLOON | | |
|---|---|---|---|---|---|---|
| | Mission target | Takeoff–landing | | Mission target/ weather | Instrument setting | Start–end |
| | | Polar 5 | Polar 6 | | | |
| **May** | | | | | | |
| 23 | Clouds above sea ice and open ocean | 0912–1425 | — | | | |
| 25 | Remote sensing of different cloud regimes | 0818–1246 | — | | | |
| 27 | A-Train overpass<br>Clouds collocated | 0758–1126<br>1305–1623 | —<br>1302–1627 | | | |
| 29 | Thin low-level clouds over sea ice | 0454–0751 | 0511–0917 | | | |
| 30 | Aircraft–PS meeting 1: Aerosol column and mapping | — | 0918–1330 | | | |
| 31 | Aircraft–PS meeting 2: Thin low-level clouds over sea ice | 1505–1857 | 1459–1903 | | | |
| **Jun** | | | | | | |
| 2 | Aircraft–PS meeting 3: Low clouds in warm air over sea ice | 0813–1355 | 0827–1409 | | | |
| 4 | Aircraft–PS meeting 4: Low clouds in warm air over sea ice | — | 1006–1539 | | | |
| 5 | Aircraft–PS meeting 5: Low clouds in warm air over sea ice | 1048–1459 | 1043–1444 | Energy fluxes/ Low clouds, snowfall | So + B1<br>(So) + B1 + B2 | 1235–1446<br>1701–2012 |
| 6 | | | | Energy fluxes/ low clouds, later fog | So + B2 + B1 | 0930–1150 |
| 7 | | | | Energy fluxes/ low clouds | So + B1 + B2 | 0920–1055 |
| | | | | Cloud remote sensing/ low clouds | Sp + B1 + Hw | 1315–1445 |

Continued on next page

with areal averages from satellite data), the cloud-top height observed from the airborne lidar is in the same range as retrieved from MODIS data. Larger differences occurred on 29 May 2017, when cirrus obscured the low-level cloud field.

Figure 3b presents the domain-averaged time series of cloud fraction for high- and low-level clouds (above and below 3-km altitude, labeled as "high" and "low," respectively, in Fig. 3b), classified for different cloud-top thermodynamic phases (labeled as "ice," "undetermined," and "liquid" in Fig. 3b) for high and low-level clouds (above and below 3-km altitude, respectively). Except for two short periods—31 May–1 June and 24–25 June 2017—the cloud cover always exceeded 70% with low-level clouds dominating. Especially between 31 May and 5 June 2017, almost no high clouds appeared in the ACLOUD/PASCAL measurement domain. The cloud phase obtained from the passive remote sensing (based on measurements of cloud-reflected, solar near-infrared radiation) is linked to the cloud top, which is why liquid-topped mixed-phase clouds can be misclassified as pure liquid water clouds (Miller et al. 2014). Therefore, the fraction of low-level liquid

**Table 2. Continued.**

| Date in 2017 | AIRCRAFT | | | TETHERED BALLOON | | |
|---|---|---|---|---|---|---|
| | | Takeoff–landing | | Mission target/ weather | Instrument setting | Start–end |
| | Mission target | Polar 5 | Polar 6 | | | |
| 8 | Aircraft–PS meeting 6: Thin broken clouds over sea ice | 0736–1251 | 0730–1320 | Energy fluxes/first clear, later fog patches, and low clouds | So + BL + B2<br>So + BL + B2<br>So + Hw + B2 | 0920–1235<br>1240–1400<br>1405–1545 |
| 9 | P5–P6 instrument comparison | 0800–0921 | 0756–0918 | Energy fluxes<br>Turbulence/overcast | So + BL + B2<br>So | 0850–0930<br>0930–1020 |
| 10 | | | | TKE, heating rates/ clear, later low clouds | Hw + BL | 1041–1115 |
| | | | | Aerosol sampling/ strong wind | Ae + Hw + BL | 1415–1800 |
| 11 | | | | TKE, heating rates/ low clouds, less wind | B2 + Hw<br>B2 + BL + Hw | 1200–1412<br>1428–1624 |
| 12 | | | | Energy fluxes/ low clouds | So + BL + B2 | 0920–1208 |
| 13 | Joint P5–P6 calibration in multilayer clouds | 1456–1655 | 1457–1716 | | | |
| 14 | Aircraft–PS meeting 7: ABL profiling | 1248–1850 | 1254–1737 | Energy fluxes/ Multilayer clouds | So + BL + B2 | 0900–1130 |
| 16 | Aircraft–PS meeting 8: Double A-Train overpass | 0445–1:01 | 0440–1031 | | | |
| 17 | Clouds above sea ice and open ocean | 0955–1525 | 1010–1555 | | | |
| 18 | Aircraft–PS meeting 9: Clouds above sea ice and open ocean | 1203–1755 | 1225–1750 | | | |
| 20 | Aircraft–PS meeting 10: ABL profiling | 0730–1355 | 0737–1327 | | | |
| 23 | Column over Ny-Ålesund | 1057–1439 | 1037–1452 | | | |
| 25 | ABL profiling in cloud-free conditions | 1109–1711 | 1103–1656 | | | |
| 26 | Aircraft Integrated Meteorological Measurement System (AIMMS-20) | — | 0833–1039 | | | |
| | ABL profiling | 1234–1517 | 1232–1448 | | | |

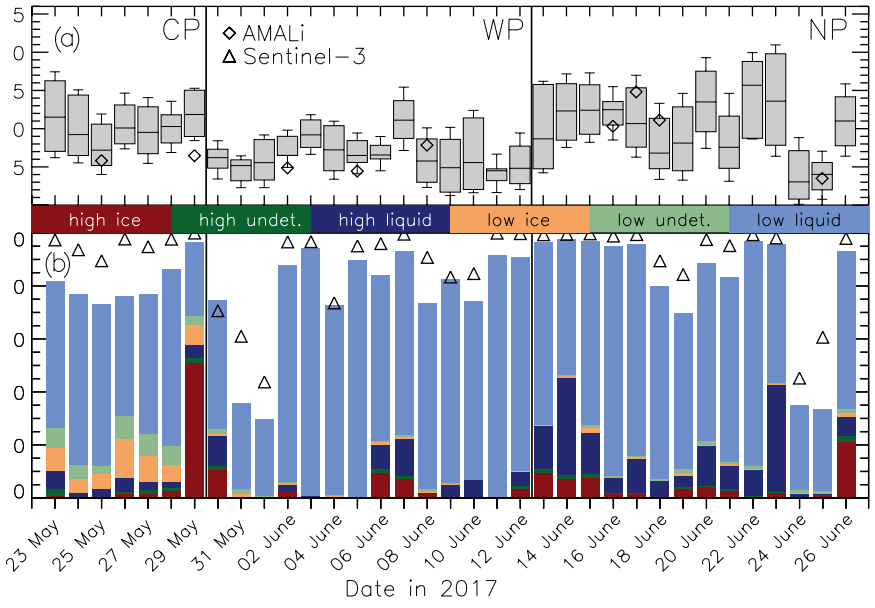


**Fig. 3. Time series of daily means of (a) cloud-top height of low-level clouds (the boxes illustrate median, 25% and 75% percentiles; the whiskers represent the standard deviation added to and subtracted from the mean cloud-top height), and (b) cloud fraction of different cloud types as derived from MODIS cloud product (Collection 6.1). The daily mean values of the top height of low-level clouds and cloud fraction were derived for the area of the airborne operation (77.5°–80°N, 0°–10.5°E and 80°–82.5°N, 0°–20°E), excluding the Svalbard archipelago. In (a) additional data from the Airborne Mobile Aerosol Lidar (AMALi) are included as open diamonds. Daily mean cloud fraction, derived from a newly developed algorithm using the *Sentinel-3* Sea and Land Surface Temperature Radiometer (SLSTR), is shown by triangles in (b). The algorithm is introduced by Jafariserajehlou et al. (2019).**

water clouds (low liquid) might be overestimated substantially in Fig. 3b. However, during the CP, a significant amount of low-level clouds was identified as the ice or undetermined phase, which indicates the influence of the flow of cold air from northerly direction on the cloud phase. During the WP and NP, only a few low-level ice clouds were identified.

Sea ice conditions. Figure 4 illustrates the change of sea ice concentration during the ACLOUD and PASCAL campaigns between the end of the CP (27–30 May 2017; Fig. 4a) and the beginning of the WP (1–4 June 2017; Fig. 4b). The CP involved northerly winds, the ice drift vectors of this period show a predominantly southwestward sea ice motion, which is typical for this region (Fig. 4a). The ice cover north of Svalbard in the Atlantic inflow region was still closed. Compared to recent years, and in particular to May 2016, the ice edge was anomalously far south in May 2017 (Tetzlaff et al. 2014), which becomes obvious from Fig. 4a. This unusually southern position of the ice edge resulted from the comparably strong positive Arctic dipole pattern, which is considered the main driver of Arctic sea ice export.

During the WP the wind turned by about 180°, pushing the ice edge northeastward (Fig. 4b), which compacted the sea ice in the western Barents Sea along the Svalbard coast, and opened ice-free areas over the Yermak Plateau north of Svalbard and in the eastern Barents Sea, and along the northern Greenland coast. The ice edge moved northward by 20–50 km (cf. to the green line in Fig. 4b). Polynyas opened along the ice edge northeast and north of Greenland. In the eastern Barents Sea and north of Franz Josef Land, large open ocean areas developed.

During the ice floe camp period (5–14 June 2017), the sea ice thickness was around 1.6–2 m, without significant changes. Snow depth was highly variable with values ranging between 0.2 and 0.4 m.

**MEASURED QUANTITIES AND MAJOR INSTRUMENTATION.** Clouds and aerosol particles as well as their interaction with atmospheric radiation and turbulence were characterized by a multitude of measured quantities and retrieved parameters, which are summarized in Table 3. Besides remote sensing instrumentation, a suite of sensors for meteorological, turbulence, radiation, microphysical, and chemical atmospheric (trace gases, aerosol particles, cloud droplets and ice crystals, precipitation) and surface (sea ice albedo, surface temperature) parameters were operated on the two AWI aircraft, the R/V *Polarstern*, the ice floe camp (including the tethered balloon), and the permanent AWIPEV research station at Ny-Ålesund. These instruments are introduced in detail in the online supplement.

**TWO ILLUSTRATIVE EXAMPLES OF COMPLEMENTARY CLOUD OBSERVATIONS.** After the general introduction of the ACLOUD and PASCAL campaigns in the "Introduction of ACLOUD

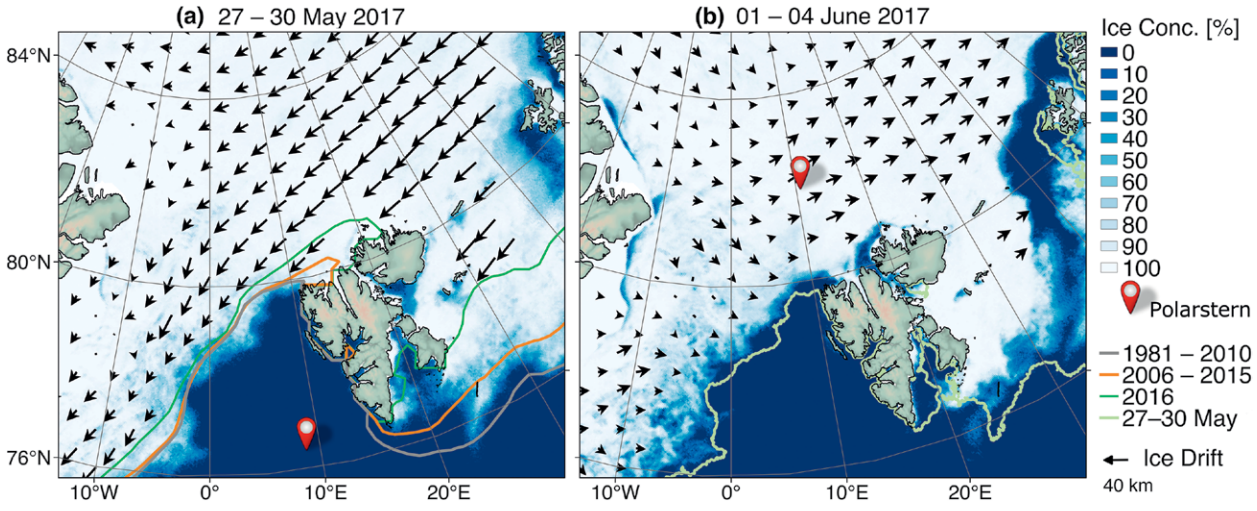


**Fig. 4. Sea ice concentration (blue to white shading) and sea ice drift (black arrows) averaged for the two periods of (a) 27–30 May and (b) 1–4 Jun 2017 in the wider ACLOUD/PASCAL region. The gray contour in (a) shows the climatological (1981–2010) 30-yr median sea ice extent for May, the orange line shows the same (median sea ice extent for May) but for the 10-yr period from 2005 to 2015, and the green line presents the averaged sea ice extent in May 2016. The green contour in (b) shows the sea ice extent from 27 to 30 May 2017 for comparison. The position of R/V *Polarstern* on (a) 30 May and (b) 4 Jun 2017 (position of ice floe camp) is marked. Data sources: Sea ice concentration data on a 3.125-km grid derived from measurements of the Advanced Microwave Scanning Radiometer 2 (AMSR2) at 89 GHz (www.seaice.uni-bremen.de; Spreen et al. 2008). Ice drift for a 2-day period on a 62.5-km grid based on AMSR2 measurements at 18.7 GHz (www.osi-saf.org; Lavergne et al. 2010). Median sea ice extent contours based on Cavalieri et al. (1996).**

and PASCAL campaigns" section and the description of the instrumentation in the section after that, two selected examples of combined measurements are discussed. The presentation aims to highlight the potential of the collocated and combined ACLOUD/PASCAL data to help constrain the Arctic cloud puzzle for future analyses.

*Collocated active remote sensing and in situ measurements*. An example of coordinated, active remote sensing and in situ measurements of cloud properties from aircraft and ship is shown in Fig. 5. The Polar 6 aircraft performed in situ measurements during double-triangle flight patterns at several low altitudes (below and within the clouds), while the Polar 5 aircraft followed the same track at higher altitudes (about 3 km) for remote sensing observations (Fig. 5a). Both aircraft were closely collocated (less than 200 m across the track distance and less than 1 min along the flight path). The time series of radar reflectivity measured by the airborne Microwave Radar/Radiometer for Arctic Clouds (MiRAC; on Polar 5) and the ship-based radar (MIRA[1] on the R/V *Polarstern*) are shown in Figs. 5b and 5c, respectively. The observed cloud was geometrically thin with a top altitude at about 400 m. This matches well with the inversion layer identified by a dropsonde (DS) released from the Polar 5 aircraft and radiosondes (RS) launched from the R/V *Polarstern* (Fig. 5d). The airborne radar MiRAC sensed the cloud almost down to the surface, whereas the ship-based radar MIRA is limited to the upper cloud column. In situ microphysical measurements averaged for each of the four legs flown with Polar 6 at different altitudes (black line in Fig. 5c) are displayed in Fig. 5e. Number concentrations of ice crystals larger than 125 $\mu$m and total water content (TWC), and images of typical cloud particles obtained by the Particle Habit Imaging and Polar Scattering (PHIPS) instrument, representative of the corresponding layers, verified the presence of ice crystals throughout the cloud and below the cloud base, while liquid droplets dominated the TWC of the cloud.

*Combined active and passive remote sensing observations*. A second example illustrates the benefit of synergetic active and passive remote sensing measurements from the Polar 5 aircraft (Fig. 6). The measurements were taken from a 3-min horizontal flight leg at an altitude of about 3.2 km. The attenuated backscatter signal from the lidar (Fig. 6a) and the radar reflectivity factor (Fig. 6b) provide vertical cross sections of the atmospheric structure, which

[1] MIRA is a proper name with no specific meaning.

yield complementary information on the vertical hydrometeor distribution.

The lidar indicates two cloud layers: the upper one ranging up to 1.3-km altitude, which partly reaches down to the top of the lower layer below 0.5-km altitude. The upper layer is optically thin and almost transparent for the lidar; the backscatter signals are much smaller than those of the lower layer. This, together with the lidar depolarization ratio (not shown) and the radar reflectivity (larger than –15 dBZ;

**Table 3. Selection of the main quantities measured and retrieved during ACLOUD/PASCAL (not complete). P5: Polar 5 aircraft; P6: Polar 6 aircraft; PS: R/V *Polarstern*; IC: ice floe camp; TB: tethered balloon; NÅ: Ny-Ålesund.**

| Cloud puzzle piece | Measured/retrieved quantities | P5 | P6 | PS | IC | TB | NÅ |
|---|---|---|---|---|---|---|---|
| Cloud properties | Top height | ✓ | | ✓ | | | ✓ |
| | Base height | | | ✓ | | | ✓ |
| | Particle number size distribution | | ✓ | | | | |
| | Droplet concentration | | ✓ | | | | |
| | LWC, IWC | | ✓ | | | | |
| | Angular scattering function | | ✓ | | | | |
| | Particle shape | | ✓ | | | | |
| | Backscattering coefficient | ✓ | | ✓ | | | ✓ |
| | Linear depolarization ratio | ✓ | | ✓ | | | ✓ |
| | Radar reflectivity factor | ✓ | | ✓ | | | ✓ |
| | Doppler velocity | ✓ | | ✓ | | | ✓ |
| | Precipitation | ✓ | ✓ | ✓ | | | ✓ |
| Aerosol impact | Particle number size distribution | | ✓ | ✓ | | | |
| | Total number concentration | | ✓ | ✓ | | | |
| | CCN, INP | | | ✓ | | | |
| | Volatility, hygroscopic growth | | | ✓ | | | |
| | Extinction, scattering, absorption coefficients | | ✓ | ✓ | | | |
| | Chemical composition | | ✓ | ✓ | | | |
| | Backscattering coefficient | ✓ | | ✓ | | | ✓ |
| | Linear depolarization ratio | ✓ | | ✓ | | | ✓ |
| | Aerosol optical depth | ✓ | | ✓ | | | ✓ |
| Atmospheric radiation | Broadband solar irradiance | ✓ | ✓ | ✓ | ✓ | ✓ | ✓ |
| | Spectral solar irradiance/radiance | ✓ | | ✓ | ✓ | ✓ | |
| | Spectral solar imaging radiance | ✓ | | | | | |
| | Broadband terrestrial irradiance | ✓ | ✓ | ✓ | ✓ | ✓ | ✓ |
| | Brightness temperature | ✓ | | | | | |
| | Microwave spectral radiance | ✓ | | ✓ | | | |
| Turbulent dynamical processes | Vertical profiles of $T$, $p$, RH | ✓ | ✓ | ✓ | ✓ | ✓ | ✓ |
| | Wind vector | ✓ | ✓ | ✓ | ✓ | ✓ | ✓ |

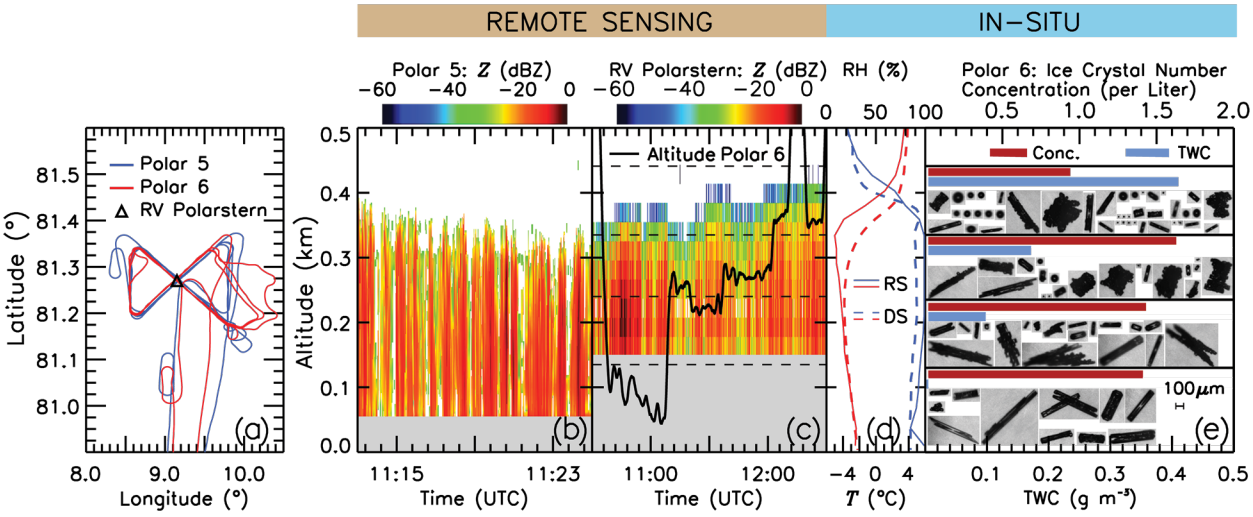


**Fig. 5. (a) Top view (horizontal projection) of the flight paths of the Polar 5 and Polar 6 aircraft (blue and red lines, respectively) and the position of R/V *Polarstern* (open triangle) on 2 Jun 2017. (b) Time series of radar reflectivity *Z* measured by the airborne MiRAC (on the Polar 5 aircraft). (c) Ship-based radar (on R/V *Polarstern*) reflectivity measurements (from MIRA), including the flight altitude of the Polar 5 aircraft (black line). (d) Vertical profile measurements (red lines for *T*, blue for RH) obtained from a DS released from the Polar 5 aircraft and RS launched from R/V *Polarstern*, and (e) microphysical in situ measurements (on the Polar 6 aircraft) representative of the four layers indicated by dashed horizontal lines in (c).**

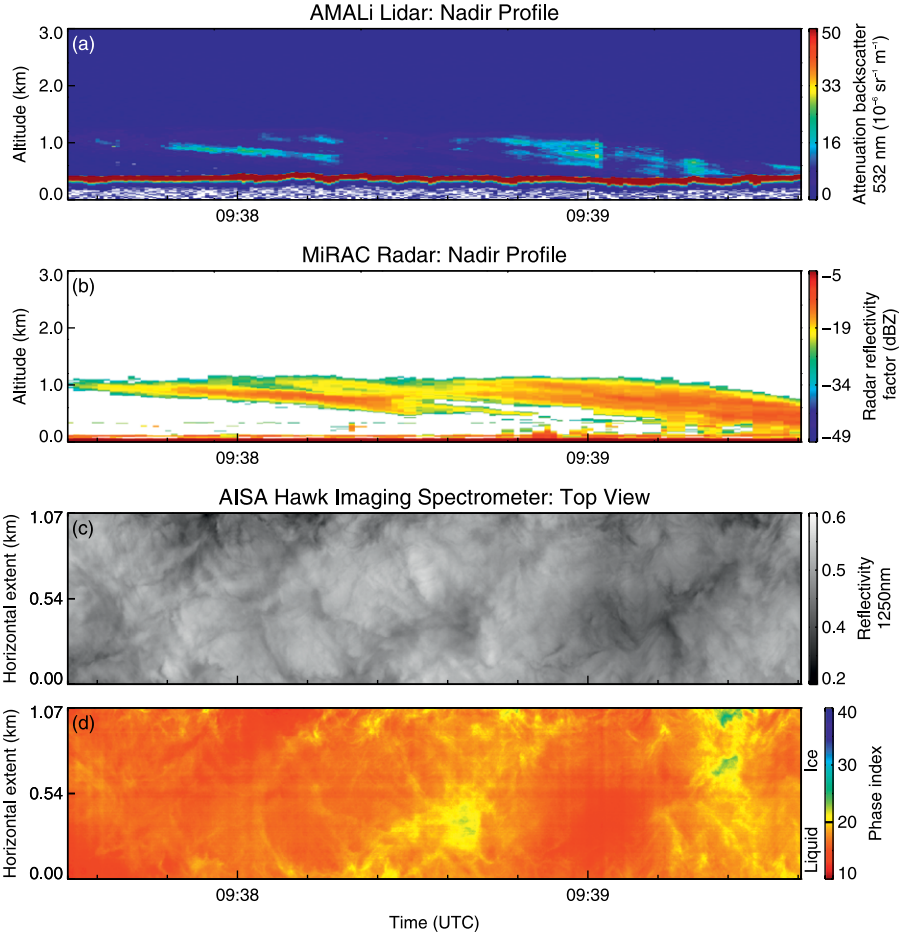


**Fig. 6. Combined measurements from the flight of the Polar 5 aircraft conducted on 27 May 2017. (a),(b) Measurements of vertical profiles by AMALi (aerosol backscatter coefficient) and MiRAC (radar reflectivity factor), respectively. (c),(d) Top views of measurements conducted with the solar near-infrared imaging hyperspectral spectrometer AISA Hawk (reflectivity and phase index). White color in (a) represents noisy signals.**

Fig. 6b), indicates that this upper cloud layer mainly consists of ice crystals. For the lower cloud layer, the lidar backscatter signal is completely attenuated in the upper part of the cloud layer, hinting at the presence of cloud liquid water. The cloud top had formed just below an inversion layer, which was detected by a dropsonde about 15 min later. The temperature in the lower cloud was below the freezing point, indicating that this lower cloud consisted mostly of supercooled water droplets. The lower cloud layer was only partly detected by the radar (Fig. 6b), which shows that the liquid water droplets at its top are small and few in number. They cause a reflectivity signal, which is partly below the radar detection limit (about −40 dB*Z* in this case).

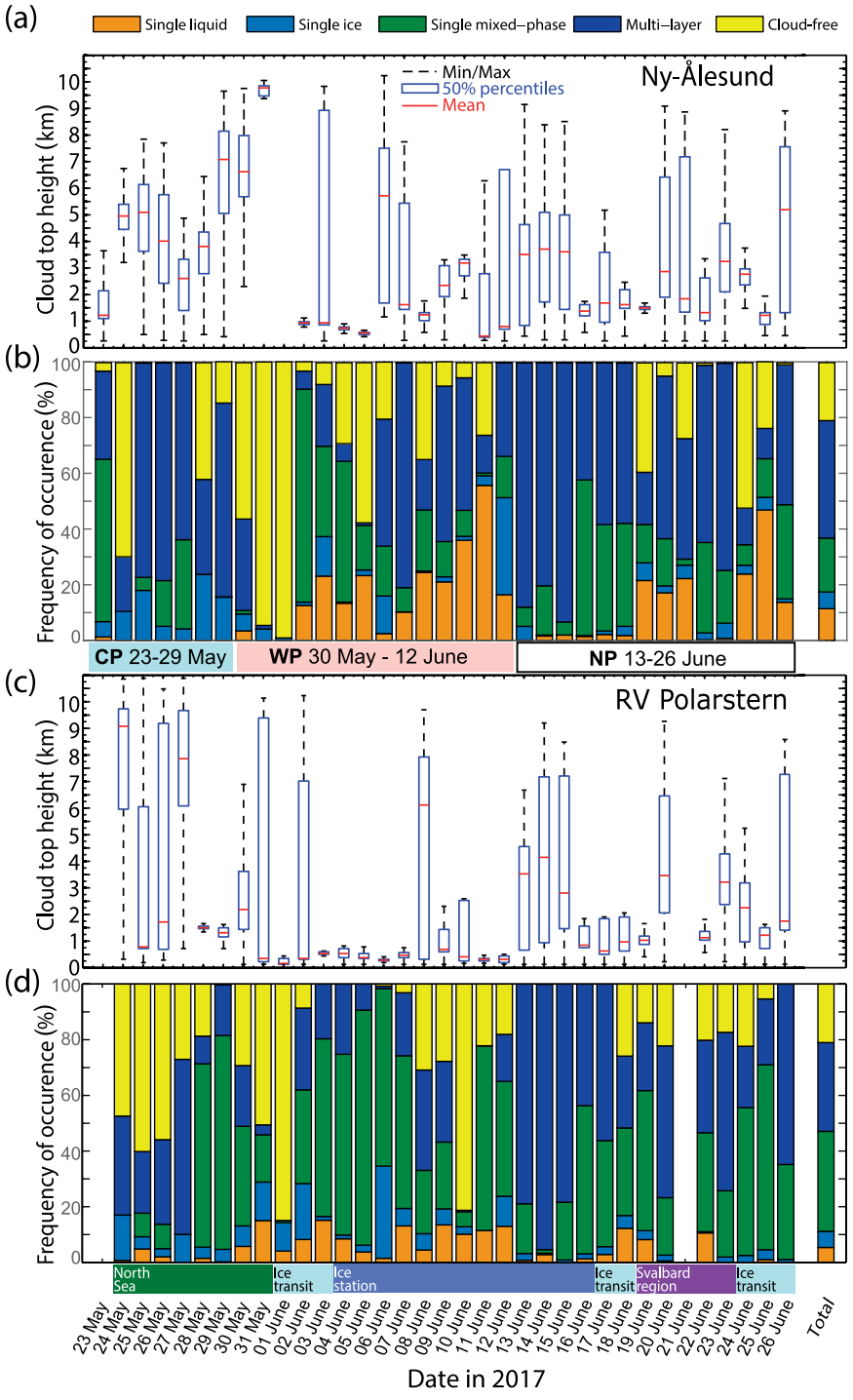


**Fig. 7. Daily averaged time series of cloud type categorization resulting from the Cloudnet algorithm for measurements taken at (a),(b) Ny-Ålesund and on (c),(d) R/V *Polarstern*, between 23 May and 26 Jun 2017. (a),(c) The statistics of the cloud-top-height distribution of all clouds shown in (b) and (d), respectively. Red horizontal bars, whisker boxes, and the dashed bars show the mean, 50% percentile, and maximum/minimum of the observed cloud-top heights of each day.**

The cloud reflectivity observations from the imaging hyperspectral Airborne Imaging Spectrometer for Applications (AISA) Hawk[2] (Fig. 6c) provide high-resolution, two-dimensional, horizontal maps of the thermodynamic phase index (Fig. 6d), which is obtained using the spectral slope of measured cloud reflectivity in the solar near-infrared spectral range (Ehrlich et al. 2008; Jäkel et al. 2013). If the phase index is larger than 20, then the cloud is composed of ice particles, while a phase index less than 20 is an indication of a liquid water cloud. In the presented example, the phase index ranges mostly below 20 except where the cloud is optically thin, indicated by a low cloud reflectivity. The phase index map is in accordance with the lidar observations showing

[2] Hawk is a proper name with no specific meaning.

a liquid cloud layer in lower altitudes. The upper ice cloud is optically thin and therefore not seen by the AISA Hawk spectrometer. It would be visible only if the lower liquid cloud layer were optically thin.

**FOUR PIECES OF THE ARCTIC CLOUD PUZZLE.** During ACLOUD/PASCAL numerous measurements have been collected to unravel some pieces of the Arctic cloud puzzle. First, results regarding four of these pieces are discussed below. These "appetizers" comprise preliminary findings and highlight selected problems and open questions. The in-depth analyses of the ACLOUD/PASCAL data will be continued.

*Puzzle piece 1: Cloud properties.* Clouds play a major role in Arctic amplification. Their macrophysical and microphysical properties determine whether they warm or cool the subcloud layer, and how strong these effects are. Local differences of cloud macrophysical properties, issues of ice formation in relatively warm clouds, and differences in ice occurrence in clouds over open ocean and sea ice are discussed in this subsection.

Cloud macrophysical properties—Local differences. Figure 7 shows data derived from surface-based profile measurements with lidar, cloud radar, and a microwave radiometer. The measurements were collected at the AWIPEV site in Ny-Ålesund and at the R/V *Polarstern*. They were utilized for daily cloud classification with the Cloudnet categorization algorithm (Illingworth et al. 2007) for the period of the ACLOUD and PASCAL campaigns (23 May–26 June 2017). Each observed profile was checked for cloud phase between cloud bottom and cloud top. When only liquid water was detected within a single cloud layer, it was considered a single-layer liquid water cloud (single liquid). The same procedure was applied to single-layer ice clouds (single ice). If both cloud liquid water and ice phases were detected in one layer, then the cloud was counted as a single-layer mixed-phase cloud (single mixed phase). Samples with more than one detected layer separated by more than two 30-m-high bins correspond to multilayer clouds (multilayer). Additionally, "cloud free" events were classified.

Figures 7a and 7b illustrate the temporal evolution of cloud-top height and type statistics as observed at Ny-Ålesund. At the end of May (during the CP), the near-surface air temperature was much lower than later during the campaigns; therefore, the single ice and single mixed-phase clouds were more frequent than in the first half of June (during the WP). During this WP the clouds occurred predominantly in the lower and midtroposphere, even though the spread of the cloud-top-height distribution was rather large. In the second half of June (during the NP), an increasing amount of single liquid clouds were observed as a result of warmer synoptic conditions. Either single mixed-phase or multilayer clouds were present throughout most of the time. These clouds were mostly formed in the lower troposphere and were likely caused by the presence of a strong temperature inversion, which is expected under high pressure conditions (Knudsen et al. 2018).

Figures 7c and 7d present corresponding results derived from measurements on the R/V *Polarstern*. The most striking feature from the comparison of the R/V *Polarstern* and the Ny-Ålesund data is that single liquid clouds were observed less frequently above the R/V *Polarstern*. In turn, more mixed-phase clouds were detected over the research vessel. This can be attributed to the location of the R/V *Polarstern*, which was 400 km north of Svalbard, where temperatures were on average lower, favoring ice formation. The R/V *Polarstern* observations were made in closed sea ice, while Ny-Ålesund had open ocean west of the coast. When the R/V *Polarstern* passed Svalbard on 31 May 2017 (120 km west of Ny-Ålesund), cloud conditions at both measurement sites were rather similar. However, in contrast to Svalbard, low and partly mixed-phase fog was present over the R/V *Polarstern* for a couple of hours. Also, it can be seen in the R/V *Polarstern* observations that fewer cloud-free periods were sampled, which can be attributed to the higher frequency of occurrence of low-level fog over the edge of the sea ice, which is also indicated by the higher frequency of occurrence of low-level clouds shown in Fig. 7c.

These data show important local differences in cloud macrophysical properties, which need to be considered in the evaluation of cloud effects on their radiative energy budget and, thus, on Arctic amplification.

Microphysical cloud properties and in-cloud temperatures—Issues of ice formation. To quantify the ranges of liquid/ice water contents and in-cloud temperatures encountered during the combined ACLOUD/PASCAL campaigns, Fig. 8 depicts probability density functions (PDFs) for liquid water content (LWC; Fig. 8a), obtained from measurements of the Nevzorov probe and a combination of the cloud droplet probe (CDP) and cloud imaging probe (CIP), as well as ice water content (IWC; Fig. 8b) and

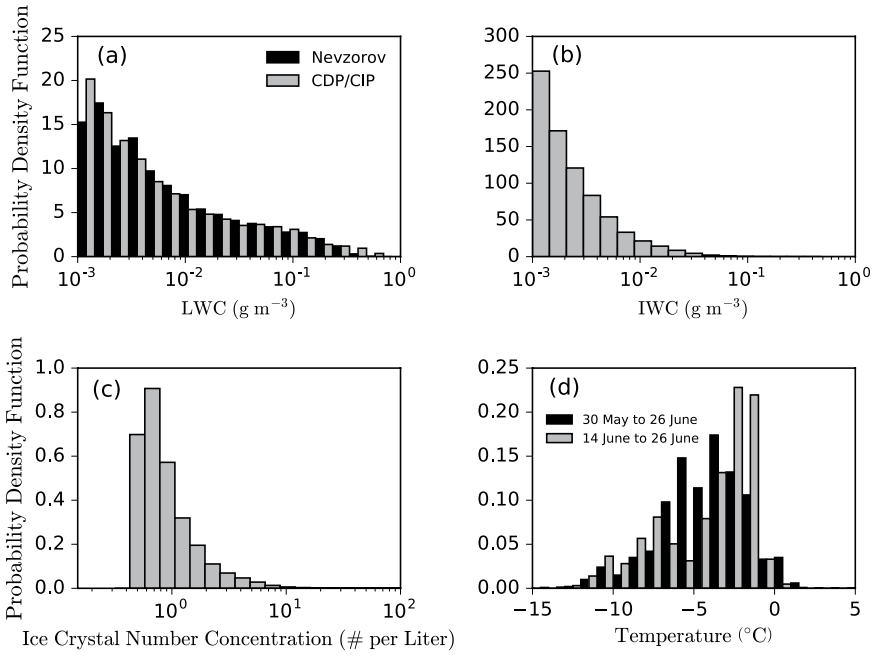


**Fig. 8. Empirical PDFs for (a) LWC, (b) IWC, (c) ice particle number concentration, and (d) *T* in clouds. These data were taken by the Nevzorov probe, CDP, and CIP installed on the Polar 6 aircraft. In total, these samples represent 13.6 h of Nevzorov measurements and 7.4 h of CDP–CIP combined data. Note that the operating periods of the two sensor types (Nevzorov and CDP–CIP) overlap only in the second half of campaign, which explains the difference in temperature PDFs.**

ice crystal number concentration (Fig. 8c) derived from CIP. In addition, Fig. 8d shows the PDF of air temperature measured in clouds. The PDFs indicate that most of the clouds sampled during the ACLOUD/PASCAL campaigns were relatively warm, with a main mode between –3° and –7°C. The LWC PDFs show an almost exponential decrease, with values extending up to 0.7 g m$^{-3}$ (Fig. 8a). Most of the IWC samples (Fig. 8b) were lower than 0.025 g m$^{-3}$, and values larger than 0.1 g m$^{-3}$ were rarely observed.

In general, clouds sampled during the ACLOUD/PASCAL campaigns consisted of supercooled liquid water droplets, with occasional large values of LWC, and quite numerous observations of small values of IWC. This complicates the evaluation of their radiative effects and roles in Arctic amplification. The cloud in situ observations have been obtained in a rather warm temperature range between –13° and 0°C (Fig. 8d). Ice crystals have been detected for all temperature ranges, although with low values of IWC. The presence of ice particles at these relatively warm temperatures raises the question with regard to the ice nucleation process, which dominated in the clouds observed during ACLOUD/PASCAL. A more thorough analysis of ice crystals' shape, size distribution in combination with in situ samples of the chemical and physical properties of ambient aerosol particles, and cloud particle residuals will be help to clarify this issue.

Presence of ice in clouds—Differences over open ocean and sea ice. To supplement the in situ microphysical measurements of ice phase in clouds and to investigate the differences in ice occurrence in clouds observed over different surface conditions, AISA Hawk measurements collected from the Polar 5 aircraft above clouds over open ocean and sea ice were analyzed and the respective statistics of the phase index were derived. Figure 9 shows the frequency of occurrence of the phase index as derived from all flight segments over clouds. The data are classified into measurements collected over open ocean and sea ice. The phase index data measured over open ocean show that the majority of the observed clouds exhibit liquid water droplets at their top. There seems to be a tendency that ice was

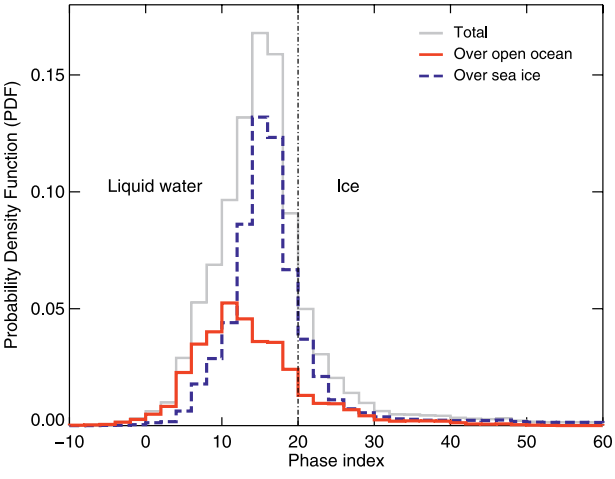


**Fig. 9. Empirical PDFs for the phase index. Total number of spectra used for the plot: 1,479,114; number of spectra collected over open ocean: 544,593; number of spectra over sea ice: 934,521; total flight time: 19.8 h; time over open ocean: 7.3 h; time spent over sea ice: 12.5 h.**

identified more often in clouds forming over sea ice. Further research will examine whether the difference in the phase index of clouds over open ocean and sea ice is real or a by-product of contamination of the cloud reflectivity by the sea ice surface.

*Puzzle piece 2: Aerosol impact on clouds.* Aerosol particles may change the radiative energy budget of the Arctic atmosphere and surface and therefore can have a direct influence on Arctic amplification. They also determine cloud formation and modify cloud properties. As such, aerosol particles can exert indirect effects on Arctic amplification via the cloud impact. Therefore, measurements of aerosol properties in the Arctic are crucial. Currently, not much data on this issue are available. In the following subsections, the respective measurements from the ACLOUD and PASCAL campaigns are presented.

AEROSOL PARTICLE CONCENTRATIONS—TOTAL, CCN, INP. Figure 10 shows a time series of the number concentrations of all aerosol particles (total), cloud condensation nuclei (CCN), and ice nucleating particles (INP) as measured at the R/V *Polarstern*. The median of the total particle number concentrations during the whole time series was 240 $cm^{-3}$ (Fig. 10a). More than 70% of the concentration was dominated by ultrafine particles (with diameters less than 100 nm), increasing up to 93% during new particle formation (NPF) events. During NPF events, the total particle number concentrations increased to an average of 2,000 $cm^{-3}$. Number concentrations were on average 2 times higher in the vicinity of Svalbard compared to times when the R/V *Polarstern* was at latitudes higher than 80°N. This indicates possible anthropogenic and natural aerosol particle sources associated with the Svalbard archipelago, but it could also be due to the proximity to open ocean versus the conditions over the sea ice pack. In open ocean there are more waves and the potential for more ocean-based production of aerosols is higher.

Figure 10b presents a time series of CCN number concentrations measured at 0.5% supersaturation (SS). This value of SS was chosen because other studies found that even small particles, with sizes less than 50 nm, can be as efficient as CCN in the Arctic at SS = 0.5% (Burkart et al. 2017; Leaitch et al. 2016). For the complete measurement period, a median of CCN concentrations of 80 $cm^{-3}$ was observed. The lowest concentrations were detected during periods within the pack ice, whereas high values occurred more frequently, but not solely, during open ocean conditions. Mauritsen et al. (2011) suggested that Arctic clouds are sometimes CCN limited, whereby

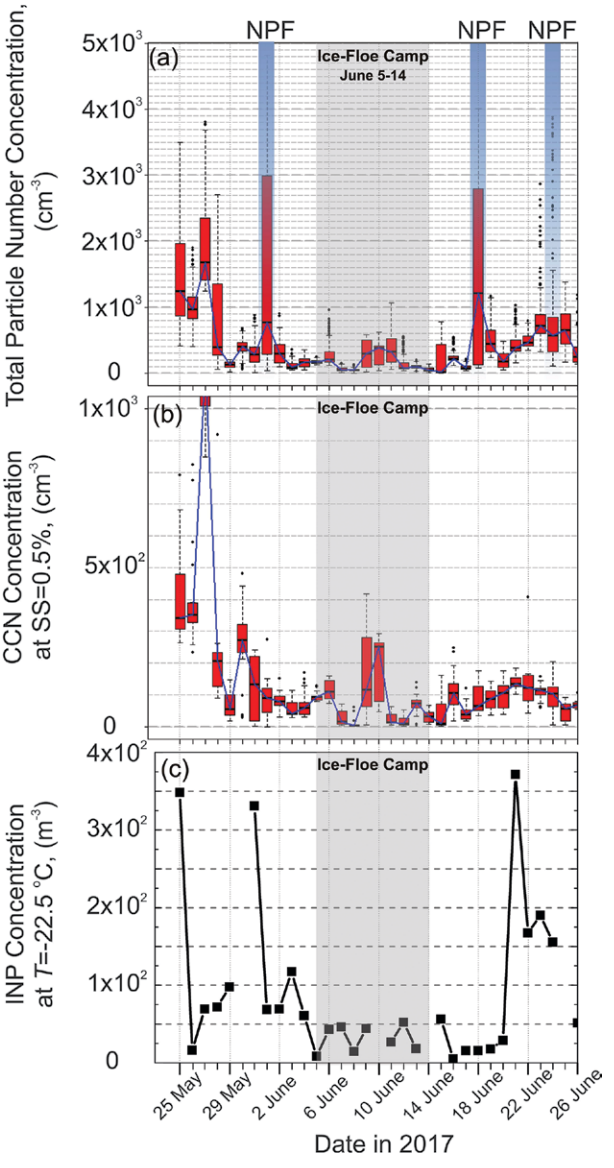


**FIG. 10. (a) Daily averaged values of total particle number concentration in the diameter range from 10 to 800 nm. NPF events (blue shading) and the time period of the ice floe camp (gray shading) are shown. (b) Daily averaged values of boxplots (red) of the CCN number concentration at 0.5% SS. (c) Time series of INP concentrations at $T$ = –22.5°C derived from polycarbonate filter. The boxplot (red) shows median (horizontal black line inside the box), interquartile range (lower and upper edges of the box), and larger/smaller values of minimum and maximum (whiskers).**

few droplets form, grow rapidly to large sizes, and fall out, leading to the dissolution of the cloud. Roughly 10% of the observed CCN number concentrations fall within this CCN-limited concentration regime (less than 10 $cm^{-3}$).

In the Arctic, where low-level mixed-phase clouds often persist while continually precipitating ice, the

presence or lack of INP at a certain temperature may play a significant role (Costa et al. 2017). Figure 10c shows a time series of INP concentrations at a temperature $T = -22.5$°C derived from measurements of polycarbonate filters with a freezing array technique. The observed concentrations are the lowest during times when the vessel was surrounded by sea ice and high during open ocean conditions. In comparison to concentrations reported by Petters and Wright (2015) for precipitation samples in North America and Europe, the concentrations measured here are at the lower end.

Particle emissions by the SML—Their role as INP. The sea surface microlayer (SML), as the direct interface between ocean and atmosphere, is suspected to be a major marine biogenic source for aerosol particles. Recent studies suggest that in the Arctic, the SML is the origin of organic biopolymers, which can be emitted into the atmosphere via bubble bursting processes (Orellana et al. 2011; Wilson et al. 2015; Irish et al. 2017). These compounds might be important in aerosol and cloud formation, in particular when acting as INP. However, the chemical nature and functionality of these SML-emitted particles is still not well known. Collocated samplings of seawater and aerosol particles in the Arctic regions are limited. Therefore, collocated samples of atmospheric aerosol particles, SML, and bulk seawater were collected in different environments (e.g., melt ponds, polynyas, open ocean). A detailed qualitative and quantitative analysis of the samples will characterize organic matter and, especially, the marine biopolymers in the diverse marine compartments, together with their INP abundance. First, results of fluorescence microscopy analysis of the SML, the bulk water, and the simultaneously collected aerosol particle samples suggest that a transfer of biogenic material from the seawater to the atmosphere might occur. This potential particle source will be investigated more thoroughly, and enrichment factors of biogenic organic matter in aerosol particles will be calculated.

Aerosol–cloud interactions—Cloud droplet residue properties over different surfaces. Cloud particles were sampled by a counterflow virtual impactor (CVI) inlet aboard the Polar 6 aircraft to determine the microphysical and chemical aerosol properties of their residuals (Ogren et al. 1985; Twohy et al. 2003). Since the Arctic clouds observed during ACLOUD/PASCAL were dominated by supercooled liquid water droplets, the residuals were mainly cloud droplet residues (CDR), not ice crystal residues. Figure 11 shows a case study of CDR characterization by different instruments connected to the CVI, with samples in low-level clouds over open ocean, drift ice [in the marginal ice zone (MIZ)], and sea ice.

The total CDR and black carbon (BC) containing CDR number concentration hardly showed any trend with respect to the underlying surface with median values around 50 and below 1 $cm^{-3}$, respectively (Fig. 11a). However, the mean diameter of the total CDR considerably changed over the different surfaces (Fig. 11b). Over open ocean the CDR mode was dominated by particles larger than 200 nm, whereas over sea ice the CDR mode was below 200 nm. In the transitional drift ice region (MIZ), the CDR number size distribution was bimodal, which indicates the influence of both open ocean and sea ice. The BC mean diameter observed in the CDR was rather constant in the range of about 100 nm. Furthermore, a slight change in the contribution of the main CDR chemical components over the different surfaces is observed (Fig. 11c). The fraction of CDR containing NaCl, organic carbon (OC), sulfate, levoglucosan, and metals was almost the same over open ocean, drift ice, and sea ice, whereas the fraction of trimethylamine (TMA) containing particles was higher over sea ice. TMA has been observed in aerosol particles over the Arctic Ocean before and is thought to be a marker for an important inner-Arctic natural biogenic particle source (Köllner et al. 2017).

During the same flight, a vertical profile of CDR properties of a low-level cloud over sea ice was measured by sampling cloud particles during five horizontal legs at different heights. Total and BC CDR number concentration and mean diameter show similar vertical patterns (Figs. 11d and 11e). The smaller CDR concentrations in Fig. 11d at lower cloud levels is due to the fact that many droplets are still small near cloud base and therefore below the CVI cutoff diameter (around 11 $\mu$m, owing to the low airspeed of the Polar 6 aircraft). A comparison to the total number concentrations of CDR showed that about 1% of the CDR was found to contain BC, which seems to reside mainly in the smaller CDR particles according to the smaller mean diameter (110 nm vs 150 nm of the total CDR). The chemical components showed a small systematic trend (with probabilities larger than 95%) with height in the cloud (Fig. 11f). The fraction of sulfate and metal containing particles increased with increasing altitude. NaCl, OC, and levoglucosan stayed rather constant and only TMA decreased with increasing height.

*Puzzle piece 3: Atmospheric radiation.* Quantifying the Arctic radiative energy budget is key for an improved

understanding of factors and processes leading to Arctic amplification. Therefore, important quantities determining the radiative energy budget and therefore influencing Arctic amplification, were measured (surface albedo, near-surface net radiation, cloud radiative forcing, heating/cooling rates). The observed data were partly compared with the output of a dynamical numerical weather prediction (NWP) model. The respective results are reported in this subsection. The measurements presented here were assembled during 15 low-level aircraft flights (average altitude about 80 m; roughly 16 flight hours; coverage of a horizontal distance of roughly 3,800 km; spatial resolution of about 3 m, that is, 20-Hz time resolution) and two tethered balloon observations.

Surface albedo and brightness temperature—Changes during sea ice melt and parameterization. Figure 12a presents a time series of broadband surface albedo derived from pyranometer aircraft measurements in cloudy and cloud-free conditions. The measurements were taken over open ocean and sea ice surfaces, with a surface albedo below 0.1 and around 0.8, respectively. The sea ice albedo gradually decreases in time as a result of the onset of melt in mid-June (Knudsen et al. 2018). This decrease is similar to what Perovich et al. (2002) have observed in their investigation of the spatial and temporal variability of wavelength-integrated albedo during the melt season. Perovich et al. (2002) measured a decreasing trend of sea ice albedo ranging between 0.85 and 0.6 from mid-April to the end of July. The beginning of the melt season is also illustrated by the brightness temperature (BT; Fig. 12b) as measured by the kelvin infrared radiation thermometer (KT-19), which gradually increases in May until the beginning of June, reaching the melting temperature by mid-June.

A specific example of aircraft-borne surface albedo measurements collected in cloud-free conditions over sea ice is presented in Fig. 13. The surface albedo at 550 nm, derived from the Spectral Modular Airborne Radiation Measurement System

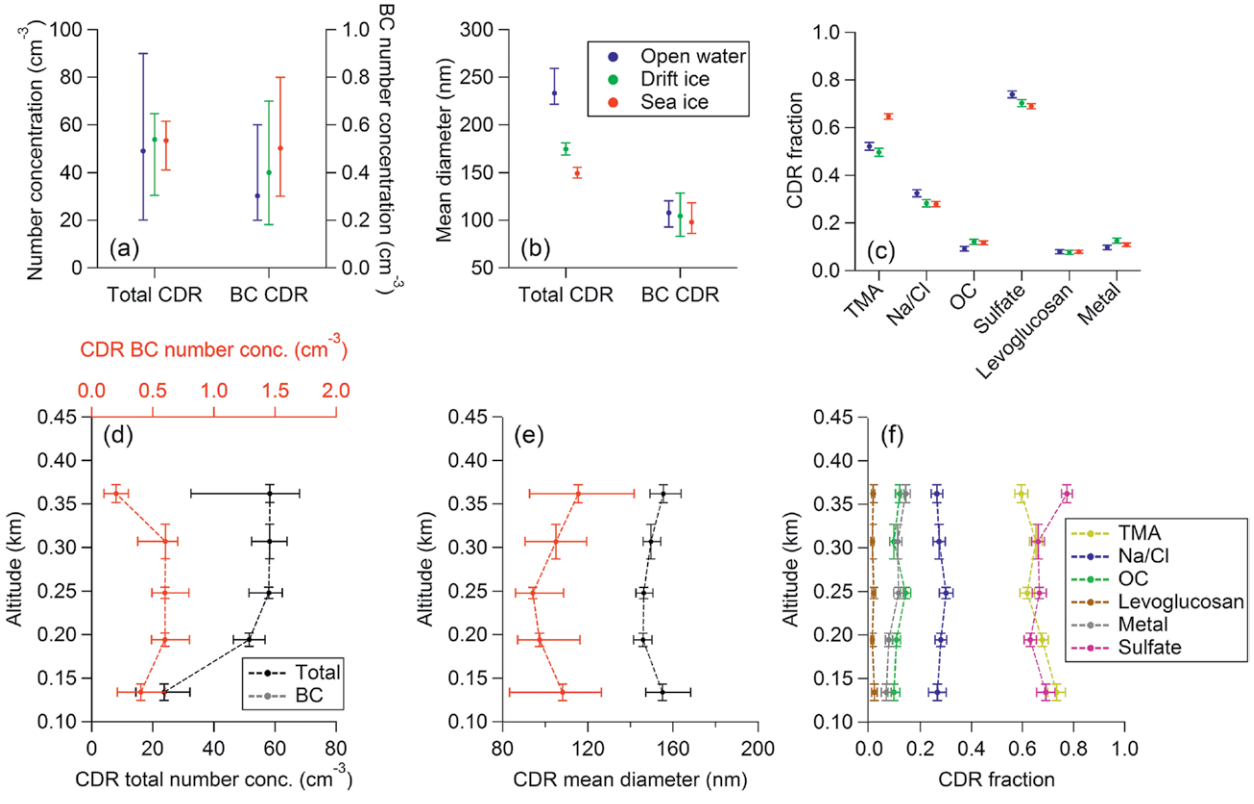


**Fig. 11. Cloud droplet residual (CDR) characterization with data from 4 Jun 2017. (a) Total and BC number concentration, (b) mean diameter, and (c) chemical composition of CDR observed in low-level clouds over open ocean, drift ice, and sea ice. Vertical profile of (d) total and BC number concentration, (e) mean diameter, and (f) chemical composition of CDR observed in a low-level cloud over sea ice. (a),(b),(d),(e) Measurements collected with Ultra-High-Sensitivity Aerosol Spectrometer (UHSAS) and single-particle soot photometer (SP2) and (c),(f) data from the Aircraft-Based Laser Ablation Aerosol Mass Spectrometer (ALABAMA) are shown; particles containing designated species; multiple particle assignment allowed. About 1,000 particles were analyzed with ALABAMA for each cloud case during this flight.**

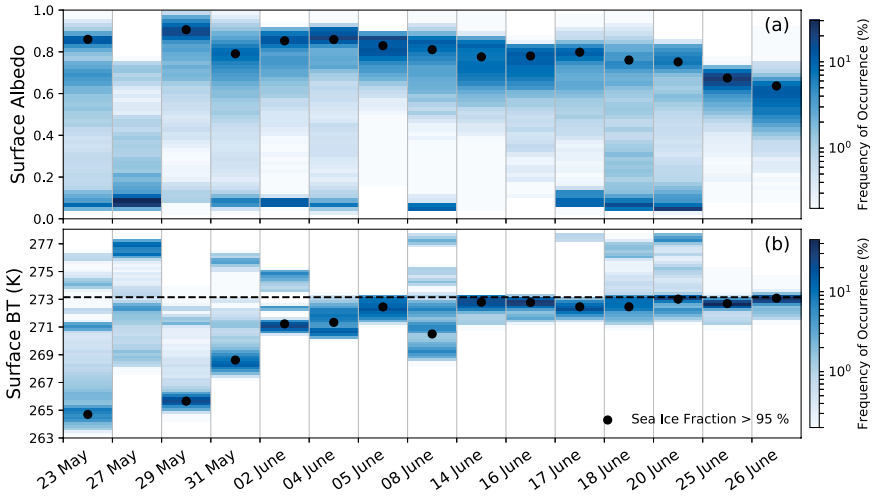


**Fig. 12. Time series of the frequency of occurrence (color coding) of (a) surface albedo as derived from the ratio of upward and downward broadband solar irradiance measurements provided by the airborne pyranometer, and (b) surface BT as measured by the KT-19. Note that the *x* axis is not continuous. The black dots indicate the respective average values of surface albedo or BT for a sea ice fraction of more than 95% (indicating homogeneous ice beneath the aircraft) as measured by the 180° fish-eye camera.**

(SMART) on board the Polar 5 aircraft, follows closely the sea ice distribution, which was obtained from the Landsat satellite at 30-m spatial resolution (Fig. 13a). In addition, a downward-looking 180° fish-eye camera on the Polar 5 aircraft took images of the surface that were used to calculate the sea ice fraction along the horizontal flight legs. The resulting relationships of the broadband and spectral (at 550-nm wavelength) surface albedo values and the sea ice fraction are shown in Fig. 13b. The figure reveals a linear increase in surface albedo, as well as an increase in albedo variability, with increasing sea ice fraction. The increased variability may be caused by two reasons: i) The surface albedo of open ocean is less variable (temporally and spectrally) than that of sea ice, which comprises a mixture of different ice types (e.g., bare or snow-covered ice); and ii) there are possibly significant three-dimensional radiative effects, which are caused by horizontally inhomogeneous distribution of ice floes and ice types with different surface albedo. Figure 13b also shows that the broadband surface albedo is lower the spectral albedo at 550-nm wavelength, which is due to sea ice being more reflective in the visible spectral range compared to the solar near-infrared. The measurements reported in Fig. 13 have the potential to resolve these issues and to improve parameterizations of surface albedo in atmospheric models.

Near-surface net radiation—Typical mode structure in measurements and simulations. Figure 14 illustrates pyrgeometer and pyranometer measurements (Figs. 14a and 14c) and corresponding collocated simulations with the atmospheric NWP Icosahedral Nonhydrostatic (ICON) model (Figs. 14b and 14d) along the low-level flight sections of the Polar 5 and Polar 6 aircraft, respectively. The number of occurrences of specific values of terrestrial and solar net (downward minus upward) irradiances is plotted (color coded) as a function of surface albedo, which discriminates different surface conditions (open ocean and sea ice).

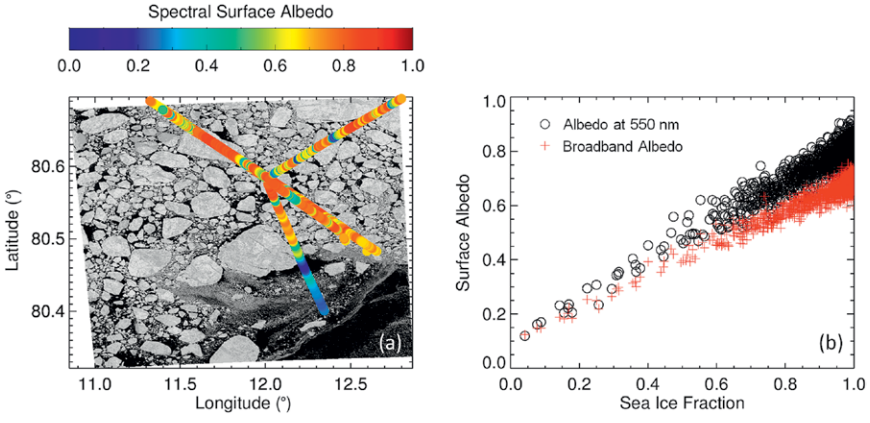


**Fig. 13. (a) Spectral surface albedo at 550-nm wavelength measured by SMART along the flight path on 25 Jun 2017, under cloud-free conditions. The corresponding Landsat image of this day is shown in the background. (b) Relationship between sea ice fraction, as derived from fish-eye images, and the broadband (red crosses) and spectral solar surface albedo at a wavelength of 550 nm (black circles).**

In the plots of the number of occurrences of the terrestrial (Fig. 14a) and solar (Fig. 14c) net irradiances, four distinct modes (relative maxima) are identified. Two cloud-related modes become obvious, shown by the red shading (indicating large values of the number of occurrences) in Fig. 14a, in the range between 0 and –20 W m$^{-2}$ for surface albedo values around 0.08 and 0.8. Another pair of modes, which is related to cloud-free atmospheric conditions, is seen between –70 and –100 W m$^{-2}$ (for surface albedo values around 0.05 and 0.7). This four-mode structure of the terrestrial net irradiance field close to the surface extends the common picture of two modes during polar night with no solar effects, which were observed in ground-based observations over one specific surface type (Shupe and Intrieri 2004; Persson et al. 1999; Stramler et al. 2011; Persson et al. 2017).

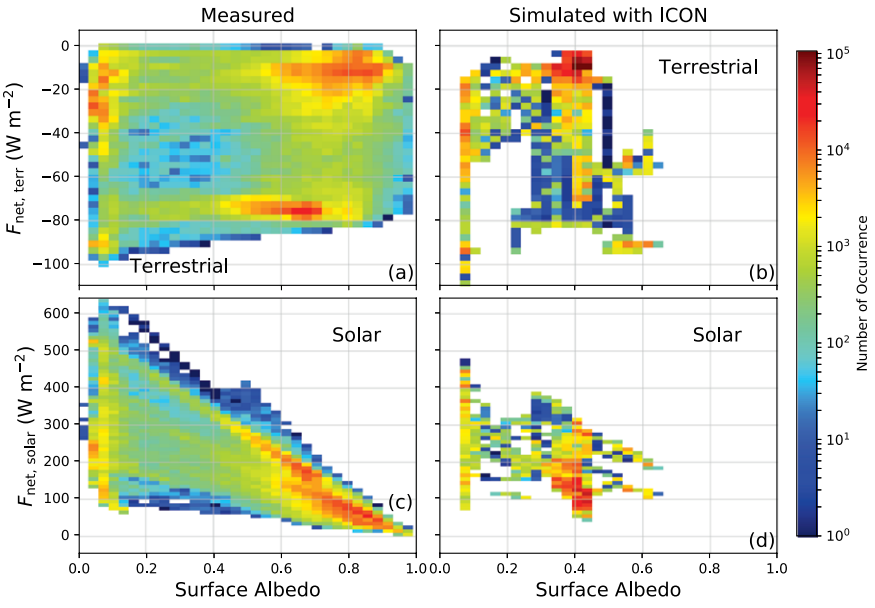


**Fig. 14. Number of occurrence of net irradiance ($F_{net} = F^{\downarrow} - F^{\uparrow}$) as a function of surface albedo. (a),(c) The results of aircraft measurements during low-level flights, and (b),(d) the respective simulations along the low-level flight sections conducted with ICON. Results for (a),(b) the terrestrial spectral range ($F_{net,terr} = F^{\downarrow}_{terr} - F^{\uparrow}_{terr}$) and (c),(d) the solar spectral range ($F_{net,solar} = F^{\downarrow}_{solar} - F^{\uparrow}_{solar}$) are shown.**

The two cloud-related modes exhibit slightly negative values of terrestrial net irradiance (between 0 and –20 W m$^{-2}$). This is because the downward terrestrial irradiance is enhanced by emission of terrestrial radiation by the clouds (up to about 320 W m$^{-2}$, not shown), whereas the upward terrestrial irradiance is almost not influenced by the clouds. Both effects result in a weak terrestrial cooling (slightly negative values of terrestrial net irradiance) at the surface. This scenario appears over open ocean (low surface albedo of less than 0.1) with slightly more negative values of terrestrial net irradiance compared to the cooling over sea ice (high surface albedo: 0.7–0.9). As a result, a typical two-mode structure of the terrestrial net irradiance field appears in cloudy conditions.

Two further modes are characteristic of the terrestrial net irradiance field in cloud-free situations. In these circumstances the downward terrestrial irradiance is much smaller ($F^{\downarrow}_{terr} \approx 220 \pm 20$ W m$^{-2}$, not shown) than the upward emission by the surface, which results in strongly negative values of the terrestrial net irradiance (cooling) in the range of $F_{net,terr} \approx -80 \pm 10$ W m$^{-2}$. The more predominant of the two modes in cloud-free conditions is obvious for measurements over sea ice with a surface albedo of about 0.6–0.7. The less pronounced second mode for cloud-free conditions appears at lower surface albedo (open ocean). The low number of occurrence for this mode is due to the flight paths, which focused on sea ice–covered areas.

The two cloud and cloud-free modes over sea ice (Figs. 14a and 14c) appear at slightly different surface albedo values (cloud-free mode at a surface albedo of 0.65, cloud mode at 0.8). This corresponds with two effects: i) the enhancement of snow albedo in overcast conditions (Wiscombe and Warren 1980) and ii) the fact that most of the cloud-free data collected over ice were sampled close to the end of the campaign, when sea ice melt reduced the surface albedo (Fig. 12a).

This four-mode structure of the net radiative field close to the surface illustrated in Figs. 14a and 14c could not be identified by previous measurements, because they almost exclusively were obtained at a fixed location with a specific local surface albedo, while the aircraft measurements during ACLOUD/PASCAL sampled different surface types.

In Figs. 14b and 14d corresponding data obtained from high-resolution simulations using the ICON model are presented. ICON was used in the regular NWP mode, as operated by the German Weather Service [Deutscher Wetterdienst (DWD); Zängl et al. 2015], but it was enhanced with a double-moment cloud microphysical scheme (Seifert and Beheng

2006). It was executed over a domain of about 1,100 × 800 km² (longitude × latitude) around the ACLOUD/PASCAL area, at a horizontal resolution of approximately 2.5 km. The model was driven by initial and boundary conditions from the operational analyses of the European Centre for Medium-Range Weather Forecasts (ECMWF) Integrated Forecast System (IFS).

As seen from Figs. 14b and 14d, the solar surface albedo from ICON ranges from less than 0.1 to about 0.7. The lower values correspond to the solar surface albedo of open ocean from the grid boxes with small or zero fractional sea ice cover. The larger values represent grid boxes with a fractional sea ice cover close to one (small or zero open ocean fraction). ICON tends to underestimate the sea ice surface albedo as compared to measurements by far. The likely most important reason is not the prognostic surface albedo parameterization used by ICON but rather the way the model is initialized. Because the ECMWF IFS data used to initialize ICON do not contain albedo fields, ICON makes a cold start and computes the sea ice surface albedo from a diagnostic formulation as a function of the sea ice surface temperature. When the sea ice surface temperature at the initialization is close to the freezing point, the diagnostic formulation yields too-low values of the surface albedo. To avoid this issue, the model should be executed one or two months prior to the target date to allow spinup of the surface fields, or to use the DWD ICON analysis data (where the time history is accounted for, and the atmospheric and surface variables are mutually consistent).

Additionally, ICON shows a tendency toward a stronger, enhanced cloud mode for optically thicker clouds. As a result, the net radiative balance simulated by ICON is too high as compared to the measurements. These deficiencies can be attributed to the underestimation of sea ice surface albedo and the ensuing errors in the surface energy budget. Generally, the surface albedo measurements from the ACLOUD/PASCAL campaigns might be used to verify and further improve the surface albedo parameterization.

Surface cloud radiative forcing—Warming or cooling by clouds. Cloud radiative forcing is calculated as the difference between airborne measurements of net solar and terrestrial irradiance and equivalent cloud-free values simulated with the radiative transfer model package libRadtran (Mayer and Kylling 2005). We have used the Discrete Ordinate Radiative Transfer model (DISORT; Stamnes et al. 1988) and the molecular absorption parameterization from Kato et al. (1999) for solar and from Gasteiger et al. (2014) for terrestrial calculations. Figure 15 compares the frequencies of occurrence of the cloud radiative forcing (solar, terrestrial, and sum of both) for a homogeneous, optically thick cloud field observed over sea ice and open ocean (Fig. 15a) and the frequencies of occurrence of an optically thin, broken cloud observed over sea ice (Fig. 15b).

Since the optically thick cloud was sampled over open ocean and sea ice, two modes in the frequency distribution of solar cloud radiative forcing appear (Fig. 15a): one for sea ice (values between –100 and 0 W m$^{-2}$) and a second mode of strong negative values obtained over open ocean. This example illustrates the effects of surface albedo on the solar cloud radiative forcing. When the surface reflects more solar radiation (high albedo), the difference in net solar radiation between cloudy and cloud-free skies is small. However, when the surface absorbs most of the downward solar radiation (low albedo), the difference between cloudy and cloud-free conditions becomes much larger. In the terrestrial spectral range, surface warming resulting

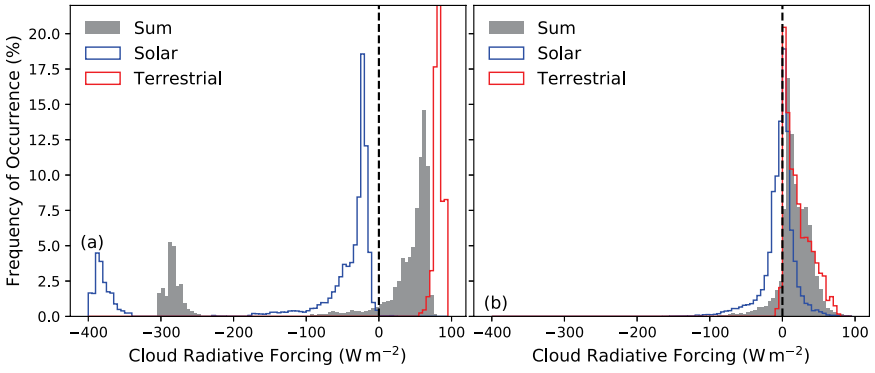


**Fig. 15. Frequency of occurrence of the cloud radiative forcing $\Delta F = F_{net,cloud} - F_{net,cloud-free}$ (difference between net irradiance measured below clouds, $F_{net,cloud}$, and an atmosphere without clouds simulated with a radiative transfer model assuming cloud-free conditions, $F_{net,cloud-free}$) for the solar and terrestrial spectral ranges, and the sum of both. (a) The results for measurements taken on 2 Jun 2017 with a quite homogeneous, optically thick cloud field. (b) Data collected below an optically thin, broken cloud observed on 31 May 2017. In (a) the maximum of the normalized frequency of the terrestrial cloud radiative forcing in the 80–85 W m$^{-2}$ bin is cut; it is 43%.**

from enhanced downward emission by the clouds is obvious in both cases. The sum of solar and terrestrial radiative forcing shows a warming for the cloud over the sea ice surface, and a cooling over the mostly absorbing open ocean.

The optically thin and broken cloud field observed over sea ice (Fig. 15b) reveals partly positive values of the solar cloud radiative forcing. This effect can be seen in situations where the direct part of solar irradiance is not attenuated, while diffuse radiation is enhanced by scattering processes in surrounding clouds. This well-known feature can enhance observed irradiance beyond a respective clear-sky state (Pfister et al. 2003) and consequently generate positive solar cloud radiative forcing. However, on average the solar cloud radiative forcing is slightly negative in Fig. 15b, while the sum of solar and terrestrial cloud radiative forcing is mostly positive (i.e., warming).

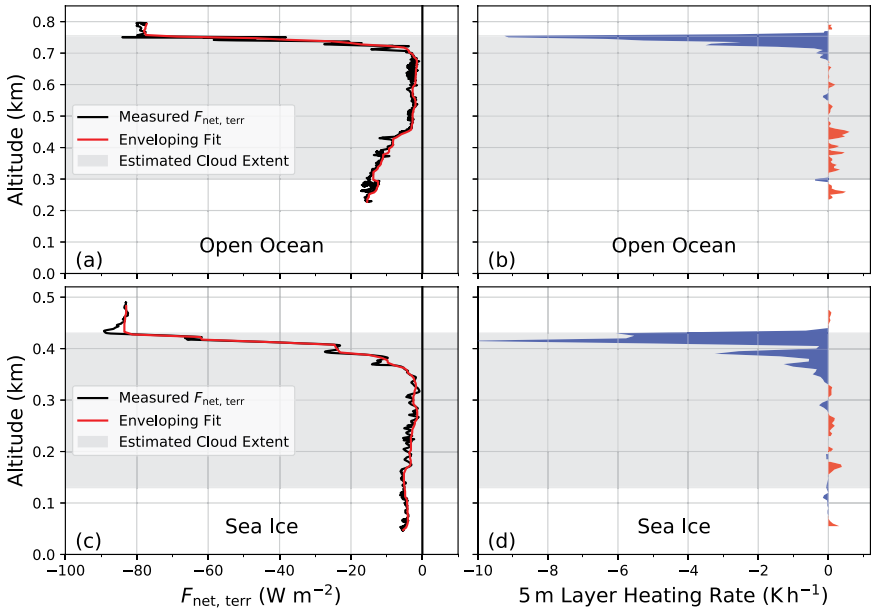


**Fig. 16. Measurements of vertical profiles of (a),(c) net terrestrial irradiance as measured with pyrgeometers ($F_{net,terr} = F^{\downarrow}_{terr} - F^{\uparrow}_{terr}$) and (b),(d) terrestrial heating rates as derived from the derivative of the terrestrial net irradiance measurements (~d$F_{net,terr}$/dz) as a function of altitude above ground z. The sampling was performed using the Polar 6 aircraft on 2 Jun 2017. In (a),(b) the results were obtained over open ocean (0948–1003 UTC, flight section short before the sea ice edge), whereas in (c),(d) the data were collected over sea ice (1022–1032 UTC). The gray boxes indicate the cloud vertical extents, estimated using Nevzorov data. The profile measurements of the terrestrial net irradiance are fitted to the red line in (a) and (c) from which the terrestrial heating rates are obtained by the first derivative as shown in (b) and (d).**

Several cloud-free measurement examples (not shown) illustrate the uncertainties of the calculated cloud radiative forcing. In cloud-free conditions, the solar cloud radiative forcing should vanish. Instead, the radiative forcing calculations show a bias of about +6.1 W m$^{-2}$ with a standard deviation of ±3.3 W m$^{-2}$. The reasons for this bias is a combination of both the uncertainty of the solar irradiance measurements and the inaccuracy of the input of the radiative transfer simulations in cloud-free conditions, possibly resulting from inadequate representation of aerosol particles. This issue requires further investigations to improve the cloud-free radiative transfer simulations.

Heating rate vertical profiles—Different surfaces and multilayer clouds. Figure 16 shows two examples of vertical profiles of terrestrial net irradiance (Figs. 16a and 16c), measured by aircraft pyrgeometers near the sea ice edge, and derived heating rates (Figs. 16b and 16d). Enhanced radiative cooling close to cloud top is obvious from Figs. 16b and 16d showing negative heating rates near the top of the cloud reaching values of up to –10 K h$^{-1}$ for both cases. The heating rate measurements above the open ocean (Figs. 16b) exhibit more of a warming tendency at the cloud base than those over sea ice (Figs. 16d) as a result of differences in surface emission. On the day of measurements (2 June 2017), a difference between the temperatures of the sea ice surface and open ocean of up to 4 K was observed (Fig. 12).

Similar pyrgeometer measurements were made from the tethered balloon (Fig. 17), which has the advantage that its measurements reach to the ground. The aircraft-borne pyrgeometer measurements do not cover altitudes less than about 30 m. In Fig. 17a a single-layer cloud was sampled, whereas in Fig. 17b the lower part of a multilayer cloud was observed. The striking difference between the two cases is the missing cloud-top cooling for the multilayer cloud case, where the warming from the upper cloud partly compensates for the cooling of the lower cloud (Shupe et al. 2013). The upper cloud blocks the ability for the supercooled liquid water droplets

of the top of the lower cloud to adequately cool to space, so essentially the top of the lower cloud cannot cool as efficiently. This shading effect might have consequences for the turbulence and life cycle of the lower cloud layer. These processes will be studied jointly with turbulence measurements in forthcoming investigations.

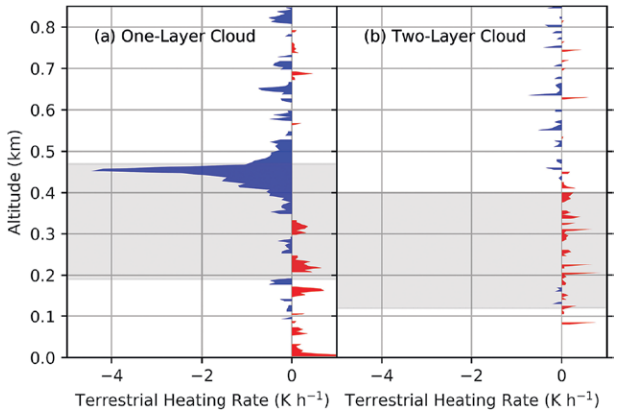


**Fig. 17. Vertical profiles of terrestrial heating rates as measured by pyrgeometers mounted on the tethered balloon. The results for (a) a single-layer cloud (5 Jun 2017) and (b) a multilayer cloud case (14 Jun 2017) are shown. The gray areas indicate the cloud layers, which were estimated based on humidity and temperature profiles, and selected camera images.**

*Puzzle piece 4: Turbulent dynamical processes.* To characterize the ABL structure by combined aircraft, balloon, and mast measurements of turbulent and radiative energy flux densities, vertical stacks of 30-km-long horizontal flight legs were realized with the Polar 5 and Polar 6 aircraft at different altitudes (below, inside, and above cloud). The stacks were aligned perpendicular to the mean wind direction at different distances downstream of the ice floe camp to cover the development of the ABL along the wind and as a function of the distance to the ice edge. The first sample was used to compare the turbulence measurements obtained from the ice floe camp (tethered balloon and mast) by flying at less than 3-km distance upstream. The almost identical turbulence instrumentation aboard the two aircraft allowed combining the datasets and therefore doubled the number of locations where ABL profiles were obtained.

Aircraft measurements. An example of measurements, obtained with the Polar 6 aircraft, is shown in Fig. 18. This case was characterized by the presence of an optically thick stratocumulus layer in the upper part of the ABL. There were no higher-level clouds over the measurement area and, thus,

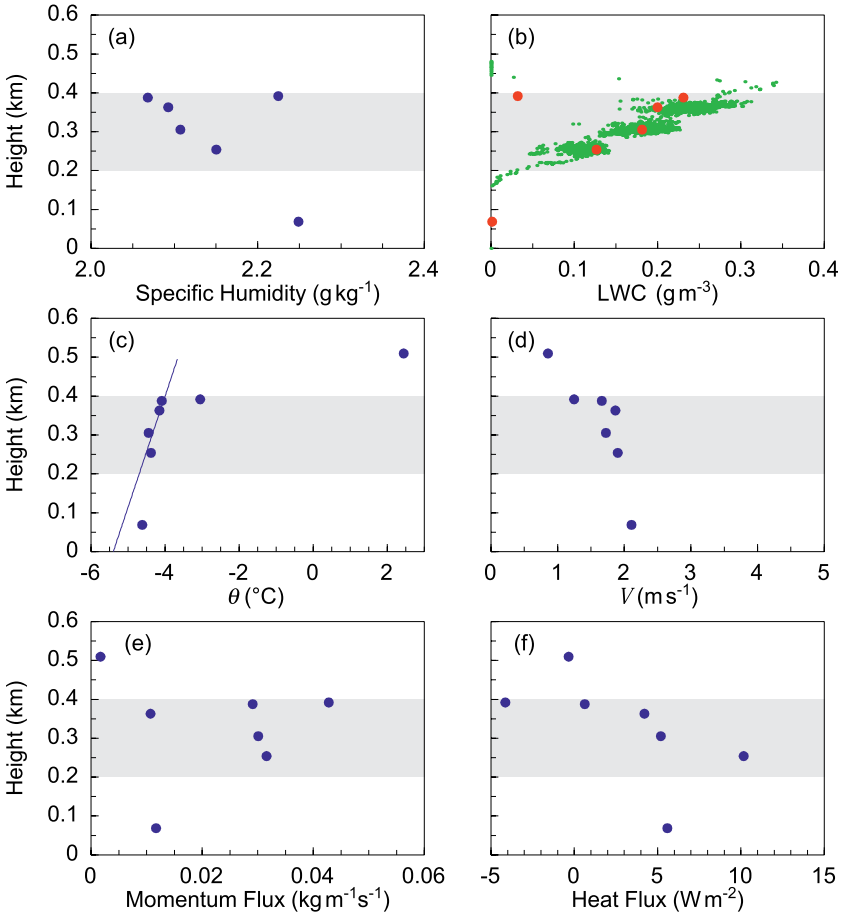


**Fig. 18. Vertical profiles of (a) specific humidity $q$; (b) LWC with green dots representing measurements from the Nevzorov probe and red dots are estimated values of LWC = $\rho \times (q_b - q)$, where $\rho$ is air density, $q_b$ is the below-cloud value of $q$; (c) potential temperature $\theta$; (d) horizontal wind velocity $V$; (e) momentum flux; and (f) heat flux. The data stem from horizontal flight legs performed during a flight of the Polar 6 aircraft on 5 Jun 2017. Each blue dot represents an average over a horizontal flight leg. The straight line in (c) indicates the wet adiabatic temperature lapse rate. The horizontal shaded areas represent the cloud layer as derived from the Nevzorov measurements [green in (b)].**

strong cloud-top radiative cooling was present (not shown).

Figure 18 depicts vertical profiles of specific humidity, LWC, potential temperature, horizontal wind speed, and fluxes of momentum and heat. The profiles suggest an ABL that is capped by a strong inversion at 390-m height that is well mixed down to the surface despite the very weak wind of only 1.5–2.5 m $s^{-1}$ throughout the ABL. The straight line in Fig. 18c indicates the wet adiabatic temperature lapse rate. Turbulent fluxes of momentum and heat have been calculated using the eddy covariance method. The cloud impact is clearly visible in both the momentum and heat flux profiles. Their maxima occur in the cloud layer.

The small positive heat fluxes in the cloud were caused by cloud radiative cooling, which generated turbulence (cold air descends, warm air rises). An important transition occurred near cloud top, which is seen in the vertical profiles of heat and in the momentum fluxes. This is due to the fact that the uppermost horizontal flight leg within the cloud occurred within the capping inversion layer, as can be seen from Figs. 18a–c. For this leg a negative heat flux was measured, as well as a maximum in the momentum flux. The negative heat flux can be explained by the entrainment of warmer air from above the ABL, while the elevated momentum flux might be due to the wind speed jump across the ABL top with stronger wind in the ABL. In this weak-wind case, cloud processes appear to dominate the vertical turbulent structure, but more work is needed to evaluate the generality of this structure.

Tethered balloon observations. Canut et al. (2016) showed that it is feasible to measure the Earth-fixed wind vector and its fluctuations with a tethered balloon-borne instrument by correcting its motion. Applying this method to the ultrasonic anemometer mounted on the tethered balloon, the Earth-fixed wind vector was measured with a frequency of 50 Hz. The balloon approach enabled a characterization of turbulence vertically throughout the entire ABL. Combined with measured fluctuations of temperature and virtual temperature, turbulent energy fluxes were calculated at fixed altitudes. For comparison with ground-based measurements, values of the wind vector, temperature, and virtual temperature were recorded on a 10-m-high meteorological mast located 30 m from the balloon launch site. The aim of the measurements was to analyze turbulent energy fluxes as a function of stratification and cloud properties.

Figure 19 illustrates two examples of vertical profile measurements using the tethered balloon payload. The examples show contrasting stratification, turbulence conditions, and cloud properties. Figures 19a–d depict a typical stratification frequently observed

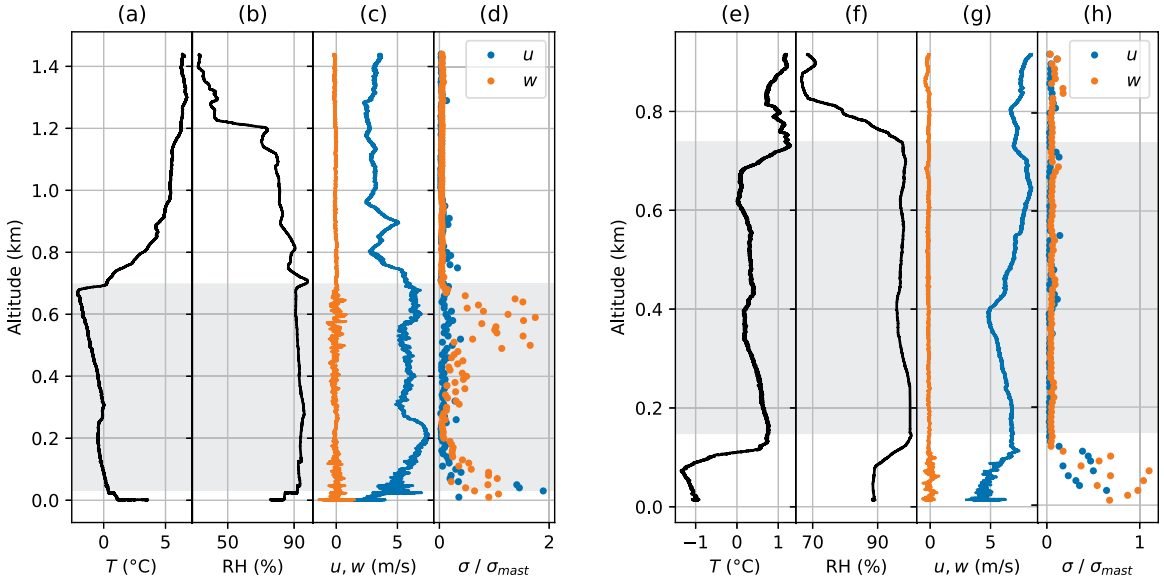


**Fig. 19. Vertical profile measurements conducted by the tethered balloon on (a)–(d) 12 and (e)–(h) 9 Jun 2017. Profiles of the following quantities are shown: (a),(e) *T*; (b),(f) RH; (c),(g) vertical wind velocity *w* (orange) and horizontal wind velocity *u* (blue); (d),(h) relative velocity variances $\sigma/\sigma_{mast}$ for vertical (orange) and horizontal (blue) wind velocities. The relative variances are estimated for 10-m-height intervals and are normalized by the respective surface velocity variances $\sigma_{mast}$ as measured at the 10-m meteorological mast. Cloud base and cloud top are estimated from RH and are plotted as shaded areas.**

during the ice floe camp period (5–14 June 2017). The main feature is a single cloud layer with a geometric thickness of about 600 m, capped by a temperature inversion layer. The horizontal wind velocity showed a pronounced maximum within the cloud. Increased turbulence, characterized by the relative variance of the wind velocity, was observed near the surface with a secondary maximum just below cloud top showing the two contributions to ABL mixing.

The second case presented in Figs. 19e–h shows a cloud located between two temperature inversion layers with two maxima for horizontal wind velocity at cloud top and below cloud base. Turbulence of horizontal and vertical winds was observed mainly below the cloud layer, in contrast to the first case, where turbulence occurred in both cloud-bottom and cloud-top regions.

**SUMMARY AND OPEN QUESTIONS.** This paper provides an overview of the combined observational field campaigns ACLOUD and PASCAL, which were performed within the framework of the German (AC)[3] project (Wendisch et al. 2017) close to Svalbard (Norway) in May and June 2017. Airborne (aircraft, tethered balloon) and ground-based (icebreaker research vessel, permanent ground station) observations have been combined to study microphysical and dynamical properties of Arctic low- and midlevel mixed-phase clouds, and their interactions with atmospheric radiation, aerosol particles, and surface properties. All of this research aims to clarify important details of the Arctic cloud puzzle. While it is certain that this wealth of new observations will contribute significantly to this goal, initial evaluations have raised further questions related to this cloud puzzle that can help to guide future analyses for ACLOUD/PASCAL as well as other research activities.

With respect to observed cloud characteristics, it is unclear why ice has been detected so frequently in comparably warm clouds observed during the ACLOUD and PASCAL campaigns. Additionally, it is necessary to clarify the influence of surface conditions (sea ice, open ocean) on cloud properties as well as the impact of spatial distribution of the ice phase in controlling cloud persistence and determining radiative forcing. Furthermore, additional observational analyses are needed to quantify how well the often observed optically thin clouds are represented by atmospheric dynamical NWP models and how well they are detected by satellites.

From a radiative point of view, the observed four-mode structure of the near-surface Arctic radiative energy budget is an essential feature of the cloud-surface interaction; further investigation is required to assess and develop realistic representations of the responsible processes in atmospheric NWP models. For example, a thorough investigation is needed of the impact of three-dimensional radiative effects in parameterizing surface albedo as a function of sea ice fraction. Also, much research is needed on the linkages among cloud microphysical properties, atmospheric heating rate profiles, and their impact on cloud dynamics and turbulence—all of which ultimately control the cloud-driven distribution of surface radiation.

On the topic of cloud dynamics, data from ACLOUD/PASCAL will help to study processes determining the persistence of mixed-phase clouds by examining questions such as, What are the sources of moisture that sustain clouds? How long can clouds survive after losing moisture by the onset of precipitation and/or entrainment of dry air? How strong is the local supply of moisture from below clouds over sea ice, for example, from leads (coupling or decoupling with the surface)?

Open questions in terms of aerosol particles include, Can particles originating from regional ocean–atmosphere coupling be discriminated from particles imported into the Arctic from the surrounding continental areas? Can local oceanic sources of aerosol influence the population and chemical composition of Arctic ice nucleating particles? Does new particle formation, despite slow observed growth rates, produce relevant concentrations of CCN?

In the coming years, ACLOUD/PASCAL observations, analyses, and related model studies will help to address these important topics.[3] Through this research, it is anticipated that substantial advances will be made in understanding Arctic cloud processes that will ultimately help to clarify the role of clouds in Arctic amplification. Data availability: The data collected during ACLOUD will be made freely available within the World Data Center PANGAEA, and will be published in Ehrlich et al. (2019): "A comprehensive in situ and remote sensing data set from the Arctic CLoud Observations Using airborne measurements during polar Day (ACLOUD) campaign" to be submitted to *Earth System Science Data*.

[3] An interjournal special issue of *Atmospheric Chemistry and Physics and Atmospheric Measurement Techniques*, Arctic Mixed-Phase Clouds as Studied during the ACLOUD/PASCAL Campaigns in the Framework of (AC)[3] (www.atmos-meas-tech.net/special_issue10_971.html), collects papers on this issue.

**ACKNOWLEDGMENTS.** We gratefully acknowledge the funding by the Deutsche Forschungsgemeinschaft (DFG, German Research Foundation) for the ArctiC Amplification: Climate Relevant Atmospheric and SurfaCe Processes, and Feedback Mechanisms (AC)³ Project Number 268020496 – TRR 172 within the Transregional Collaborative Research Center. The LaMP acknowledges the support of the Pollution in the Arctic System (PARCS) project funded by the Chantier Arctique of the Centre National de la Recherche Scientifique–Institut National des Sciences de l'Univers (CNRS-INSU). Dmitrii Mironov from DWD is acknowledged for his helpful comments with respect to the use of the ICON model. The authors are grateful to AWI for providing and operating the two aircraft, the ship, and the AWIPEV facilities during the ACLOUD and PASCAL campaigns. We thank the crews of the Polar 5 and Polar 6 aircraft, as well as the crew of the R/V *Polarstern* (in particular the aircraft pilots and the captain of the ship), the technicians of the aircraft and the ship, and the scientific and technical personnel of the AWIPEV station in Ny-Ålesund for the excellent technical and logistical support. The generous funding of the flight hours for ACLOUD and the ship time for PASCAL in the framework of the R/V *Polarstern* cruise PS106 (Expedition Grant AWI-PS106-00) by AWI is greatly appreciated.

## REFERENCES

Bierwirth, E., and Coauthors, 2013: Optical thickness and effective radius of Arctic boundary-layer clouds retrieved from airborne nadir and imaging spectrometry. *Atmos. Meas. Tech.*, **6**, 1189–1200, https://doi.org/10.5194/amt-6-1189-2013.

Brock, C. A., and Coauthors, 2011: Characteristics, sources, and transport of aerosols measured in spring 2008 during the Aerosol, Radiation, and Cloud Processes affecting Arctic Climate (ARCPAC) Project. *Atmos. Chem. Phys.*, **11**, 2423–2453, https://doi.org/10.5194/acp-11-2423-2011.

Brümmer, B., D. Schröder, G. Müller, G. Spreen, A. Jahnke-Bornemann, and J. Launiainen, 2008: Impact of a Fram Strait cyclone on ice edge, drift, divergence, and concentration: Possibilities and limits of an observational analysis. *J. Geophys. Res.*, **113**, C12003, https://doi.org/10.1029/2007JC004149.

Burkart, J., and Coauthors, 2017: Organic condensation and particle growth to CCN sizes in the summertime marine Arctic is driven by materials more semivolatile than at continental sites. *Geophys. Res. Lett.*, **44**, 10 725–10 734, https://doi.org/10.1002/2017GL075671.

Canut, G., F. Couvreux, M. Lothon, D. Legain, B. Piguet, A. Lampert, W. Maurel, and E. Moulin, 2016: Turbulence fluxes and variances measured with a sonic anemometer mounted on a tethered balloon. *Atmos. Meas. Tech.*, **9**, 4375–4386, https://doi.org/10.5194/amt-9-4375-2016.

Cavalieri, D. J., and Coauthors, 1983: MIZEX West: Bering Sea Marginal Ice Zone Experiment. *Eos, Trans. Amer. Geophys. Union*, **64**, 578–579, https://doi.org/10.1029/EO064i040p00578.

——, C. L. Parkinson, P. Gloersen, and H. J. Zwally, 1996: Sea ice concentrations from Nimbus-7 SMMR and DMSP SSM/I-SSMIS passive microwave data, version 1.1. NASA National Snow and Ice Data Center Distributed Active Archive Center, accessed 22 March 2019, https://doi.org/10.5067/8GQ8LZQVL0VL.

Cohen, J., and Coauthors, 2014: Recent Arctic amplification and extreme mid-latitude weather. *Nat. Geosci.*, **7**, 627–637, https://doi.org/10.1038/ngeo2234.

——, K. Pfeiffer, and J. A. Francis, 2018: Warm Arctic episodes linked with increased frequency of extreme winter weather in the United States. *Nat. Commun.*, **9**, 869, https://doi.org/10.1038/s41467-018-02992-9.

Costa, A., and Coauthors, 2017: Classification of Arctic, midlatitude and tropical clouds in the mixed-phase temperature regime. *Atmos. Chem. Phys.*, **17**, 12 219–12 238, https://doi.org/10.5194/acp-17-12219-2017.

Curry, J. A., and Coauthors, 2000: FIRE Arctic Clouds Experiment. *Bull. Amer. Meteor. Soc.*, **81**, 5–30, https://doi.org/10.1175/1520-0477(2000)081<0005:FACE>2.3.CO;2.

Delanoe, J., A. Protat, O. Jourdan, J. Pelon, M. Papazzoni, R. Dupuy, J.-F. Gayet, and C. Jouan, 2013: Comparison of airborne in situ, airborne radar–lidar, and spaceborne radar–lidar retrievals of polar ice cloud properties sampled during the POLARCAT campaign. *J. Atmos. Oceanic Technol.*, **30**, 57–73, https://doi.org/10.1175/JTECH-D-11-00200.1.

Ehrlich, A., E. Bierwirth, M. Wendisch, J.-F. Gayet, G. Mioche, A. Lampert, and J. Heintzenberg, 2008: Cloud phase identification of Arctic boundary-layer clouds from airborne spectral reflection measurements: Test of three approaches. *Atmos. Chem. Phys.*, **8**, 7493–7505, https://doi.org/10.5194/acp-8-7493-2008.

——, M. Wendisch, E. Bierwirth, J.-F. Gayet, G. Mioche, A. Lampert, and B. Mayer, 2009: Evidence of ice crystals at cloud top of Arctic boundary-layer mixed-phase clouds derived from airborne remote sensing. *Atmos. Chem. Phys.*, **9**, 9401–9416, https://doi.org/10.5194/acp-9-9401-2009.

Freese, D., and C. Kottmeier, 1998: Radiation exchange between stratus clouds and polar marine surfaces. *Bound.-Layer Meteor.*, **87**, 331–356, https://doi.org/10.1023/A:1000992701127.

Freud, E., R. Krejci, P. Tunved, R. Leaitch, Q. T. Nguyen, A. Massling, H. Skov, and L. Barrie, 2017: Pan-Arctic aerosol number size distributions: Seasonality and transport patterns. *Atmos. Chem. Phys.*, **17**, 8101–8128, https://doi.org/10.5194/acp-17-8101-2017.

Gasteiger, J., C. Emde, B. Mayer, R. Buras, S. Buehler, and O. Lemke, 2014: Representative wavelengths absorption parameterization applied to satellite channels and spectral bands. *J. Quant. Spectrosc. Radiat. Transfer*, **148**, 99–115, https://doi.org/10.1016/j.jqsrt.2014.06.024.

Gryanik, V. M., and J. Hartmann, 2002: A turbulence closure for the convective boundary layer based on a two-scale mass-flux approach. *J. Atmos. Sci.*, **59**, 2729–2744, https://doi.org/10.1175/1520-0469(2002)059<2729:ATCFTC>2.0.CO;2.

——, ——, S. Raasch, and M. Schröter, 2005: A refinement of the Millionshchikov quasi-normality hypothesis for convective boundary layer turbulence. *J. Atmos. Sci.*, **62**, 2632–2638, https://doi.org/10.1175/JAS3457.1.

Hartmann, J. N., C. Kottmeier, and C. Wamser, 1992: Radiation and Eddy Flux Experiment 1991 (REFLEX I). Berichte zur Polarforschung 105, 72 pp.

——, C. Kottmeier, C. Wamser, and E. Augstein, 1994: Aircraft measured atmospheric momentum, heat and radiation fluxes over arctic sea ice. *The Polar Oceans and Their Role in Shaping the Global Environment*, *Meteor. Monogr.*, Vol. 85, Amer. Geophys. Union, 443–454, https://doi.org/10.1029/GM085p0443.

——, and Coauthors, 1999: Arctic Radiation and Turbulence Interaction Study (ARTIST). Alfred-Wegener-Institute for Polar and Marine Research, http://epic.awi.de/26485/.

Illingworth, A. J., and Coauthors, 2007: CLOUDNET: Continuous evaluation of cloud profiles in seven operational models using ground-based observations. *Bull. Amer. Meteor. Soc.*, **88**, 883–898, https://doi.org/10.1175/BAMS-88-6-883.

Intrieri, J. M., C. W. Fairall, M. D. Shupe, P. O. G. Persson, E. L Andreas, P. S. Guest, and R. E. Moritz, 2002: An annual cycle of Arctic surface cloud forcing at SHEBA. *J. Geophys. Res.*, **107**, 8039, https://doi.org/10.1029/2000JC000439.

Irish, V. E., and Coauthors, 2017: Ice-nucleating particles in Canadian Arctic sea-surface microlayer and bulk seawater. *Atmos. Chem. Phys.*, **17**, 10 583–10 595, https://doi.org/10.5194/acp-17-10583-2017.

Jacob, D. J., and Coauthors, 2010: The Arctic Research of the Composition of the Troposphere from Aircraft and Satellites (ARCTAS) mission: Design, execution, and first results. *Atmos. Chem. Phys.*, **10**, 5191–5212, https://doi.org/10.5194/acp-10-5191-2010.

Jafariserajehlou, S., L. Mei, M. Vountas, V. Rozanov, J. P. Burrows, and R. Hollmann, 2019: A cloud identification algorithm over the Arctic for use with AATSR–SLSTR measurements. *Atmos. Meas. Tech.*, **12**, 1059–1076, https://doi.org/10.5194/amt-2018-231.

Jäkel, E., J. Walther, and M. Wendisch, 2013: Thermodynamic phase retrieval of convective clouds: Impact of sensor viewing geometry and vertical distribution of cloud properties. *Atmos. Meas. Tech.*, **6**, 539–547, https://doi.org/10.5194/amt-6-539-2013.

Jeffries, M. O., J. E. Overland, and D. K. Perovich, 2013: The Arctic shifts to a new normal. *Phys. Today*, **66**, 35–40, https://doi.org/10.1063/PT.3.2147.

Jones, H. M., and Coauthors, 2018: Summertime Arctic aircraft measurements during ACCACIA. *Atmos. Chem. Phys. Discuss.*, https://doi.org/10.5194/acp-2018-283.

Jung, T., and Coauthors, 2016: Advancing polar prediction capabilities on daily to seasonal time scales. *Bull. Amer. Meteor. Soc.*, **97**, 1631–1647, https://doi.org/10.1175/BAMS-D-14-00246.1.

Kato, S., T. Ackerman, J. Mather, and E. Clothiaux, 1999: The *k*-distribution method and correlated-*k* approximation for a shortwave radiative transfer model. *J. Quant. Spectrosc. Radiat. Transfer*, **62**, 109–121, https://doi.org/10.1016/S0022-4073(98)00075-2.

Knudsen, E. M., and Coauthors, 2018: Meteorological conditions during the ACLOUD/PASCAL field campaign near Svalbard in early summer 2017. *Atmos. Chem. Phys.*, **18**, 17 995–18 022, https://doi.org/10.5194/acp-18-17995-2018.

Knust, R., 2017: Polar research and supply vessel POLARSTERN operated by the Alfred-Wegener-Institute. *J. Large-Scale Res. Facil.*, **3**, A119, https://doi.org/10.17815/jlsrf-3-163.

Köllner, F., and Coauthors, 2017: Particulate trimethylamine in the summertime Canadian high Arctic lower troposphere. *Atmos. Chem. Phys.*, **17**, 13 747–13 766, https://doi.org/10.5194/acp-17-13747-2017.

Kurtz, N., J. Richter-Menge, S. Farrell, M. Studinger, J. Paden, J. Sonntag, and J. Yungel, 2013: IceBridge airborne survey data support Arctic sea ice predictions. *Eos, Trans. Amer. Geophys. Union*, **94**, 41–49, https://doi.org/10.1002/2013eo040001.

Kottmeier, C., J. Hartmann, C. Wasmer, A. Bochert, C. Lüpkes, D. Freese, and W. Cohrs, 1994: Radiation and Eddy Flux Experiment 1993 (REFLEX II). Berichte zur Polarforschung 133, 62 pp.

Lavergne, T., S. Eastwood, Z. Teffah, H. Schyberg, and L.-A. Breivik, 2010: Sea ice motion from low-resolution satellite sensors: An alternative method

and its validation in the Arctic. *J. Geophys. Res.*, **115**, C10032, https://doi.org/10.1029/2009JC005958.

Law, K. S., and Coauthors, 2014: Arctic air pollution: New insights from POLARCAT-IPY. *Bull. Amer. Meteor. Soc.*, **95**, 1873–1895, https://doi.org/10.1175/BAMS-D-13-00017.1.

Leaitch, W. R., and Coauthors, 2016: Effects of 20–100 nm particles on liquid clouds in the clean summertime Arctic. *Atmos. Chem. Phys.*, **16**, 11 107–11 124, https://doi.org/10.5194/acp-16-11107-2016.

Leck, C., E. K. Bigg, D. S. Covert, J. Heintzenberg, W. Maenhaut, E. D. Nilsson, and A. Wiedensohler, 1996: Overview of the atmospheric research program during the International Arctic Ocean Expedition of 1991 (IAOE-91) and its scientific results. *Tellus*, **48B**, 136–155, https://doi.org/10.3402/tellusb.v48i2.15833.

Lloyd, G., and Coauthors, 2015: Observations and comparisons of cloud microphysical properties in spring and summertime Arctic stratocumulus clouds during the ACCACIA campaign. *Atmos. Chem. Phys.*, **15**, 3719–3737, https://doi.org/10.5194/acp-15-3719-2015.

Macke, A., and H. Flores, 2018: The expeditions PS106/1 and 2 of the Research Vessel POLARSTERN to the Arctic Ocean in 2017. Alfred Wegener Institute for Polar and Marine Research Reports on Polar and Marine Research 719, 171 pp., https://doi.org/10.2312/BzPM_0719_2018.

Mauritsen, T., and Coauthors, 2011: An Arctic CCN-limited cloud-aerosol regime. *Atmos. Chem. Phys.*, **11**, 165–173, https://doi.org/10.5194/acp-11-165-2011.

Mayer, B., and A. Kylling, 2005: Technical note: The libRadtran software package for radiative transfer calculations—Description and examples of use. *Atmos. Chem. Phys.*, **5**, 1855–1877, https://doi.org/10.5194/acp-5-1855-2005.

McFarquhar, G. M., and Coauthors, 2011: Indirect and Semi-Direct Aerosol Campaign. *Bull. Amer. Meteor. Soc.*, **92**, 183–201, https://doi.org/10.1175/2010BAMS2935.1.

Miller, N. B., M. D. Shupe, C. J. Cox, V. P. Walden, D. D. Turner, and K. Steffen, 2015: Cloud radiative forcing at Summit, Greenland. *J. Climate*, **28**, 6267–6280, https://doi.org/10.1175/JCLI-D-15-0076.1.

Miller, S. D., Y.-J. Noh, and A. K. Heidinger, 2014: Liquid-top mixed-phase cloud detection from shortwave-infrared satellite radiometer observations: A physical basis. *J. Geophys. Res. Atmos.*, **119**, 8245–8267, https://doi.org/10.1002/2013JD021262.

MIZEX Group, 1986: MIZEX East 83/84: The summer marginal ice zone program in the Fram Strait/Greenland Sea. *Eos, Trans. Amer. Geophys. Union*, **67**, 513–517, https://doi.org/10.1029/EO067i023p00513.

Morrison, H., G. de Boer, G. Feingold, J. Harrington, M. D. Shupe, and K. Sulia, 2012: Resilience of persistent Arctic mixed-phase clouds. *Nat. Geosci.*, **5**, 11–17, https://doi.org/10.1038/ngeo1332.

Neuber, R., 2006: A multi-disciplinary Arctic research facility: From the Koldewey - Rabot - Corbel - Stations to the AWI-IPEV research base on Spitsbergen. *Polarforschung*, **73**, 117–123.

Ogren, J., J. Heintzenberg, and R. Charlson, 1985: In situ sampling of clouds with a droplet to aerosol converter. *Geophys. Res. Lett.*, **12**, 121–124, https://doi.org/10.1029/GL012i003p00121.

Onarheim, I. H., T. Eldevik, L. H. Smedsrud, and J. C. Stroeve, 2018: Seasonal and regional manifestation of Arctic sea ice loss. *J. Climate*, **31**, 4917–4932, https://doi.org/10.1175/JCLI-D-17-0427.1.

Orellana, M. V., P. A. Matrai, C. Leck, C. D. Rauschenberg, A. M. Lee, and E. Coz, 2011: Marine microgels as a source of cloud condensation nuclei in the high Arctic. *Proc. Natl. Acad. Sci. USA*, **108**, 13 612–13 617, https://doi.org/10.1073/pnas.1102457108.

Perovich, D. K., T. C. Grenfell, B. Light, and P. V. Hobbs, 2002: Seasonal evolution of the albedo of multiyear Arctic sea ice. *J. Geophys. Res.*, **107**, 8044, https://doi.org/10.1029/2000JC000438.

——, ——, J. A. Richter-Menge, B. Light, W. B. Tucker III, and H. Eicken, 2003: Thin and thinner: Sea ice mass balance measurements during SHEBA. *J. Geophys. Res.*, **108**, 8050, https://doi.org/10.1029/2001JC001079.

Persson, P. O. G., T. Uttal, J. M. Intrieri, C. W. Fairall, E. L. Andreas, and P. S. Guest, 1999: Observations of large thermal transitions during the Arctic night from a suite of sensors at SHEBA. *Third Symp. on Integrated Observing Systems*, Dallas, TX, Amer. Meteor. Soc., J5.3, https://ams.confex.com/ams/older/99annual/abstracts/477.htm.

——, M. D. Shupe, D. Perovich, and A. Solomon, 2017: Linking atmospheric synoptic transport, cloud phase, surface energy fluxes, and sea-ice growth: Observations of midwinter SHEBA conditions. *Climate Dyn.*, **49**, 1341–1364, https://doi.org/10.1007/s00382-016-3383-1.

Petters, M. D., and T. P. Wright, 2015: Revisiting ice nucleation from precipitation samples. *Geophys. Res. Lett.*, **42**, 8758–8766, https://doi.org/10.1002/2015GL065733.

Pfister, G., R. McKenzie, J. Liley, A. Thomas, B. Forgan, and C. Long, 2003: Cloud coverage based on all-sky imaging and its impact on surface solar irradiance. *J. Appl. Meteor.*, **42**, 1421–1434, https://doi.org/10.1175/1520-0450(2003)042<1421:CCBOAI>2.0.CO;2.

Pithan, F., and Coauthors, 2018: Role of air-mass transformations in exchange between the Arctic and mid-latitudes. *Nat. Geosci.*, **11**, 805–812, https://doi.org/10.1038/s41561-018-0234-1.

Raschke, E., S. Kinne, W. B. Rossow, P. W. Stackhouse, and M. Wild, 2016: Comparison of radiative energy flows in observational datasets and climate modeling. *J. Appl. Meteor. Climatol.*, **55**, 93–117, https://doi.org/10.1175/JAMC-D-14-0281.1.

Richter-Menge, J., J. E. Overland, J. T. Mathis, and E. Osborne, Eds., 2017: Arctic report card 2017. NOAA, www.arctic.noaa.gov/Report-Card.

Rösel, A., and L. Kaleschke, 2012: Exceptional melt pond occurrence in the years 2007 and 2011 on the Arctic sea ice revealed from MODIS satellite data. *J. Geophys. Res.*, **117**, C05018, https://doi.org/10.1029/2011JC007869.

Screen, J. A., and Coauthors, 2018: Consistency and discrepancy in the atmospheric response to Arctic sea-ice loss across climate models. *Nat. Geosci.*, **11**, 155–163, https://doi.org/10.1038/s41561-018-0059-y.

Sedlar, J., and M. D. Shupe, 2014: Characteristic nature of vertical motions observed in Arctic mixed-phase stratocumulus. *Atmos. Chem. Phys.*, **14**, 3461–3478, https://doi.org/10.5194/acp-14-3461-2014.

Seifert, A., and K. D. Beheng, 2006: A two-moment cloud microphysics parameterization for mixed-phase clouds. Part 1: Model description. *Meteor. Atmos. Phys.*, **92**, 45–66, https://doi.org/10.1007/s00703-005-0112-4.

Serreze, M. C., and R. G. Barry, 2011: Processes and impacts of Arctic amplification: A research synthesis. *Global Planet. Change*, **77**, 85–96, https://doi.org/10.1016/j.gloplacha.2011.03.004.

Shupe, M. D., and J. M. Intrieri, 2004: Cloud radiative forcing of the Arctic surface: The influence of cloud properties, surface albedo, and solar zenith angle. *J. Climate*, **17**, 616–628, https://doi.org/10.1175/1520-0442(2004)017<0616:CRFOTA>2.0.CO;2.

——, S. Y. Matrosov, and T. Uttal, 2006: Arctic mixed-phase cloud properties derived from surface-based sensors at SHEBA. *J. Atmos. Sci.*, **63**, 697–711, https://doi.org/10.1175/JAS3659.1.

——, P. O. G. Persson, I. M. Brooks, M. Tjernström, J. Sedlar, T. Mauritsen, S. Sjogren, and C. Leck, 2013: Cloud and boundary layer interactions over the Arctic sea ice in late summer. *Atmos. Chem. Phys.*, **13**, 9379–9400, https://doi.org/10.5194/acp-13-9379-2013.

Smith, W. M., and Coauthors, 2017: Arctic Radiation-IceBridge Sea and Ice Experiment (ARISE): The Arctic radiant energy system during the critical seasonal ice transition. *Bull. Amer. Meteor. Soc.*, **98**, 1399–1426, https://doi.org/10.1175/BAMS-D-14-00277.1.

Sotiropoulou, G., and Coauthors, 2016: Atmospheric conditions during the Arctic Clouds in Summer Experiment (ACSE): Contrasting open water and sea ice surfaces during melt and freeze-up seasons. *J. Climate*, **29**, 8721–8744, https://doi.org/10.1175/JCLI-D-16-0211.1.

Spreen, G., L. Kaleschke, and G. Heygster, 2008: Sea ice remote sensing using AMSR-E 89-GHz channels. *J. Geophys. Res.*, **113**, C02S03, https://doi.org/10.1029/2005JC003384.

Stamnes, K., S. Tsay, W. Wiscombe, and K. Jayaweera, 1988: A numerically stable algorithm for discrete-ordinate-method radiative transfer in multiple scattering and emitting layered media. *Appl. Opt.*, **27**, 2502–2509, https://doi.org/10.1364/AO.27.002502.

Stephens, G., D. Winker, J. Pelon, C. Trepte, D. Vane, C. Yuhas, T. L'Ecuyer, and M. Lebsock, 2018: *CloudSat* and *CALIPSO* within the A-Train: Ten years of actively observing the Earth system. *Bull. Amer. Meteor. Soc.*, **99**, 569–581, https://doi.org/10.1175/BAMS-D-16-0324.1.

Stramler, K., A. D. Del Genio, and W. B. Rossow, 2011: Synoptically driven Arctic winter states. *J. Climate*, **24**, 1747–1762, https://doi.org/10.1175/2010JCLI3817.1.

Stroeve, J. C., M. C. Serreze, M. M. Holland, J. E. Kay, J. Maslanik, and A. P. Barrett, 2012: The Arctic's rapidly shrinking sea ice cover: A research synthesis. *Climatic Change*, **110**, 1005–1027, https://doi.org/10.1007/s10584-011-0101-1.

Tetzlaff, A., C. Lüpkes, G. Birnbaum, J. Hartmann, T. Nygard, and T. Vihma, 2014: Brief communication: Trends in sea ice extent north of Svalbard and its impact on cold air outbreaks as observed in spring 2013. *Cryosphere*, **8**, 1757–1762, https://doi.org/10.5194/tc-8-1757-2014.

——, ——, and J. Hartmann, 2015: Aircraft-based observations of atmospheric boundary-layer modification over Arctic leads. *Quart. J. Roy. Meteor. Soc.*, **141**, 2839–2856, https://doi.org/10.1002/qj.2568.

Tjernström, M., C. Leck, P. Persson, M. Jensen, S. Oncley, and A. Targino, 2004: The summertime Arctic atmosphere: Meteorological measurements during the Arctic Ocean Experiment (AOE-2001). *Bull. Amer. Meteor. Soc.*, **85**, 1305–1321, https://doi.org/10.1175/BAMS-85-9-1305.

——, and Coauthors, 2014: The Arctic Summer Cloud Ocean Study (ASCOS): Overview and experimental design. *Atmos. Chem. Phys.*, **14**, 2823–2869, https://doi.org/10.5194/acp-14-2823-2014.

——, and Coauthors, 2015: Warm-air advection, air mass transformation and fog causes rapid ice melt. *Geophys. Res. Lett.*, **42**, 5594–5602, https://doi.org/10.1002/2015GL064373.

Twohy, C., J. Strapp, and M. Wendisch, 2003: Performance of a counterflow virtual impactor in the NASA Icing Research Tunnel. *J. Atmos. Oceanic Technol.*, **20**, 781–790, https://doi.org/10.1175/1520-0426(2003)020<0781:POACVI>2.0.CO;2.

Uttal, T., and Coauthors, 2002: Surface Heat Budget of the Arctic Ocean. *Bull. Amer. Meteor. Soc.*, **83**, 255–275, https://doi.org/10.1175/1520-0477(2002)083<0255:SHBOTA>2.3.CO;2.

——, and Coauthors, 2016: International Arctic Systems for Observing the Atmosphere: An International Polar Year legacy consortium. *Bull. Amer. Meteor. Soc.*, **97**, 1033–1056, https://doi.org/10.1175/BAMS-D-14-00145.1.

Verlinde, J., and Coauthors, 2007: The Mixed-Phase Arctic Cloud Experiment. *Bull. Amer. Meteor. Soc.*, **88**, 205–222, https://doi.org/10.1175/BAMS-88-2-205.

Walsh, J. E., 2014: Intensified warming of the Arctic: Causes and impacts on middle latitudes. *Global Planet. Change*, **117**, 52–63, https://doi.org/10.1016/j.gloplacha.2014.03.003.

Wendisch, M., P. Yang, and A. Ehrlich, 2013: Amplified climate changes in the Arctic: Role of clouds and atmospheric radiation. *Sitzungsber. Saechs. Akad. Wiss. Leipzig, Math.-Naturwiss. Kl.*, **132** (3), 1–34.

——, and Coauthors, 2017: Understanding causes and effects of rapid warming in the Arctic. *Eos, Trans. Amer. Geophys. Union*, **98**, 22–26, https://doi.org/10.1029/2017EO064803.

Wesche, C., D. Steinhage, and U. Nixdorf, 2016: Polar aircraft Polar5 and Polar6 operated by the Alfred Wegener Institute. *J. Large-Scale Res. Facil.*, **2**, A87, https://doi.org/10.17815/jlsrf-2-153.

Wilson, T. W., L. A. Ladino, and J. M. Murray, 2015: A marine biogenic source of atmospheric ice-nucleating particles. *Nature*, **525**, 234–238, https://doi.org/10.1038/nature14986.

Wiscombe, W., and S. Warren, 1980: A model for the spectral albedo of snow. Part I. Pure snow. *J. Atmos. Sci.*, **37**, 2712–2733, https://doi.org/10.1175/1520-0469(1980)037<2712:AMFTSA>2.0.CO;2.

Zängl, G., D. Reinert, P. Rípodas, and M. Baldauf, 2015: The ICON (ICOsahedral Non-hydrostatic) modelling framework of DWD and MPI-M: Description of the non-hydrostatic dynamical core. *Quart. J. Roy. Meteor. Soc.*, **141**, 563–579, https://doi.org/10.1002/qj.2378.

# Science at Your Fingertips

**AMS Journals are now optimized for viewing on your mobile device.**

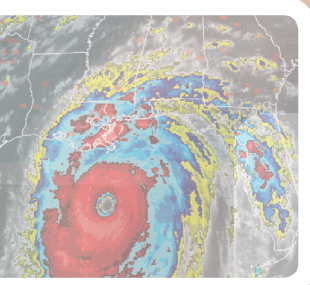


**Access journal articles, monograph titles, and BAMS content using your iOS, Android, or Blackberry phone, or tablet.**

**Features include:**

- **Saving articles for offline reading**
- **Sharing of article links via email and social networks**
- **Searching across journals, authors, and keywords**

**And much more...**

**Scan code to connect to journals.ametsoc.org**

AMERICAN METEOROLOGICAL SOCIETY